Ore Geology Reviews 138 (2021) 104342

Contents lists available at ScienceDirect

Ore Geology Reviews

journal homepage: www.elsevier.com/locate/oregeorev

Enrichment of rare earth elements in the early Cambrian Zhijin phosphorite deposit, SW China: Evidence from francolite micro-petrography and geochemistry

Zeyang Zhang [a,b,c], Yuhang Jiang [a,b,*], Hecai Niu [a,b], Jieqi Xing [a,b,c], Shuang Yan [a,b], Ao Li [a,b,c], Qiang Weng [a,b,c], Xiaochen Zhao [a,b,c]

[a] CAS Key Laboratory of Mineralogy and Metallogeny/Guangdong Provincial Key Laboratory of Mineral Physics and Materials, Guangzhou Institute of Geochemistry, Chinese Academy of Sciences, Guangzhou 510640, China
[b] CAS Center for Excellence in Deep Earth Science, Guangzhou 510640, China
[c] University of Chinese Academy of Sciences, Beijing 100049, China

ARTICLE INFO

Keywords:
Transmission electron microscopy
Early cambrian
Zhijin REE-rich phosphorite
Nanoscale francolite
Hydrothermal sedimentary

ABSTRACT

The Zhijin phosphorite deposit is a giant early Cambrian rare earth element (REE) deposit, with particular enrichment in heavy REEs, and is of high economic significance. The REEs of the deposit occur almost entirely in apatite, which, on the basis of petrographic characteristics, can be divided into francolite grains (90%), amorphous apatite, and phosphate fossils. In this paper, we report an investigation into francolite grains in different types of phosphorite from ore sections of the Zhijin deposit. Detailed petrographic and transmission electron microscopy observations reveal that the francolite grains are composed of nano-apatite crystals measuring 120–160 nm long. Trace-element contents of pyrite and whole-rock geochemical indicators (such as Cr/Zr and V/Ni ratios and Th/U–Co/Ni plots) suggest that the Zhijin phosphorite formed in an anoxic hydrothermal sedimentary environment. However, the negative Ce/Ce* and Eu/Eu* anomalies indicate that the diagenetic environment of the francolite grains was oxidic. Different diagenetic redox environments and the presence of transportation fractures in francolite grains identified under back-scattered electron imaging reveal that the francolite grains underwent prolonged abrasion and transportation in seawater before sedimentation. Petrographic observations and laser ablation–mass spectrometry element surface scanning analyses indicate that the REEs are uniformly distributed in nano-apatite in isomorphic form, and no nano-inclusions or REE minerals were found, implying that late mineralization was not the cause of REE enrichment. The higher $(La/Yb)_N$ ratios of francolite grains relative to seawater indicate that the francolite grains captured abundant REEs during the early diagenetic stage. We infer that prolonged exposure to seawater and the high specific surface area of francolite grains are the key factors that led to the enrichment in REEs. Combining the timing of the metallogenic epoch (543 Ma), Sr–Nd isotopic data, and the Y/Ho ratio, which is close to those of modern seawater, indicates that the REEs were sourced from paleo-seawater. Paleogeographic information suggests that during the early Cambrian, extensive continental collisions caused great amounts of continental weathering products to enter the paleo-ocean, leading to the production of abundant amounts of hydrothermal–sedimentary phosphorus and REEs in shallow seas, thus forming an ideal sedimentary environment for generating the REE resources of the Zhijin phosphorite deposit.

1. Introduction

Phosphorite is a non-renewable economic resource and is consequently a geological research topic of high interest. The contents of rare earth elements (REEs) in global phosphorites exceed those of most known REE deposits, meaning that the utilization of associated REE resources in phosphorite deposits has recently attracted more attention (Radhika et al., 2011; Emsbo et al., 2015). It is generally considered that

* Corresponding author at: CAS Key Laboratory of Mineralogy and Metallogeny/Guangdong Provincial Key Laboratory of Mineral Physics and Materials, Guangzhou Institute of Geochemistry, Chinese Academy of Sciences, Guangzhou 510640, China.
E-mail address: jiangyuhang@gig.ac.cn (Y. Jiang).

https://doi.org/10.1016/j.oregeorev.2021.104342
Received 13 April 2021; Received in revised form 23 June 2021; Accepted 30 June 2021
Available online 10 July 2021
0169-1368/© 2021 Published by Elsevier B.V.

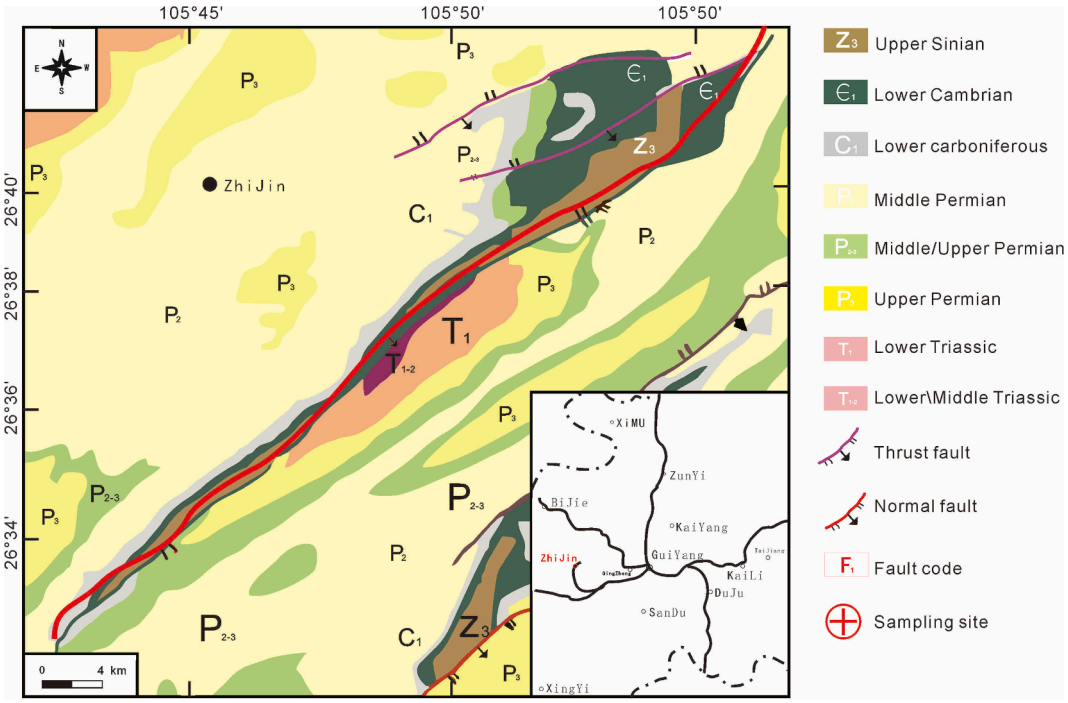

Fig. 1. Geological sketch map of the Zhijin mining region, after Zhou et al. (2019).

REEs enter apatite during the earliest stage of diagenesis, thus faithfully recording the REE composition of seawater at the time of deposition (Elderfield and Pagett, 1986; Wright et al., 1987; Piper et al., 1988; Picard et al., 2002; Lécuyer et al., 2004; Martin and Scher, 2004), with many studies interpreting normalized REE patterns similar to those of modern seawater as major elements (Elderfield and Pagett, 1986; Wright et al., 1987; Piper et al., 1988; Picard et al., 2002; Martin and Scher, 2004). Variation in REE abundance in phosphorite is attributed mainly to lithofacies, grain size, burial time, and burial depth (McArthur and Walsh, 1984; Ilyin, 1998; Shields and Stille, 2001; Shields and Webb, 2004). Some geologists have considered that REE content is the product of post-deposition alteration, whereby REEs are redistributed between detrital and authigenic phases during the process of attaining diagenetic equilibrium between phosphate solid and pore water (McArthur and Walsh, 1984; Ilyin, 1998; Shields and Stille, 2001; Shields and Webb, 2004; Bright et al., 2009). The primary impetus for the study of REEs in phosphates has been the investigation of phosphate genesis and paleo-marine chemistry (Piper, 1999; Lécuyer et al., 2004; Emsbo et al., 2015). However, the geological processes controlling the content of REEs in phosphorites remain uncertain, and the source of REEs in phosphorite is also unclear, meaning that further studies of typical deposits are needed to elucidate phosphorite REE deposit genesis.

It has been suggested that apatite plays an important role in the REE enrichment mechanism of phosphorites and that it forms within the upper part of the sediment pile during early diagenesis (e.g., Peru continental margin) or at/near the sediment–water interface (e.g., Miocene Monterey Bay Formation; Follmi, 1996; Gadd et al., 2016). The REEs in phosphate-rich rocks are almost entirely contained in apatite (Jarvis et al., 1994; Emsbo et al., 2015), and this mineral is known to faithfully record the environment of diagenesis and to reveal the mechanism of REE enrichment (Reynard et al., 1999; Harlov and FÖrster, 2003; Shields and Webb, 2004; Li and Zhou, 2015; Fan et al., 2016).

The Zhijin phosphorite deposit developed in phosphorus-bearing strata of the Yangtze platform during the early Cambrian, an important phosphorus-forming period during which >150 phosphorite deposits formed globally (Holland, 2005; Emsbo et al., 2015). The Zhijin deposit contains proven phosphate ore reserves of 13.48×10^8 t and rare earth oxide reserves of 144.6×10^4 t, and it is a typical REE-rich phosphorite marine sedimentary deposit (Gui and Zhen, 1987; Zhang et al., 2003; Zhang et al., 2007a; Zhang et al., 2007b; Liu et al., 2016; Guo et al., 2017; Xu et al., 2019). Abundant fossils are preserved in the Zhijin phosphorite, revealing that the development of the phosphate deposit was accompanied by biological prosperity (Broecker, 1982; Runnegar, 2000). Previous studies have confirmed that the occurrence of the deposit was controlled by stratigraphy, lithofacies, and paleogeography (Zhang et al., 2003; Zhang et al., 2007a; Zhang et al., 2007b; Mao et al., 2014; Liu et al., 2016). Clastic structure and tidal bedding indicate that the phosphorite formed in a turbulent tidal environment (Zhang et al., 2007a; Zhang et al., 2007b; Chen et al., 2010; Guo et al., 2017).

Regarding the enrichment mechanism of REEs in Zhijin phosphorite, several studies have demonstrated that only negligible REEs are absorbed by clay mineral grains, with the dominant amounts of REEs occurring in apatite (Zhang et al., 2007a; Zhang et al., 2007b; Chen et al., 2010; Xu et al., 2019). The phosphate mineral in Zhijin phosphorite is termed as "collophanite", and it is considered that REEs in phosphorite occur in isomorphic form, displaying the characteristics of MREE enrichment and right-dipping patterns of HREEs in element variation diagrams (Gui and Zhen, 1987; Zhang et al., 2007a; Zhang et al., 2007b; Liu et al., 2016; Lou and Gu, 2019). However, the mineral compositions or micro-petrography of phosphate aggregates of the Zhijin deposit have not been studied, meaning that the ultra-microscopic petrographic characteristics of REE-hosting apatite in the deposit, the enrichment mechanism of REEs, and the source of REEs are poorly understood.

In this paper, we present a detailed study of the ultra-microscopic petrographic characteristics of apatite (francolite grains) by transmission electron microscopy (TEM) to establish the occurrence of REEs in phosphorite. On the basis of whole-rock and francolite grain geochemistry, we reveal the diagenetic processes of francolite grains and the sedimentary environment of the phosphorite. We also constrain the REE source of the deposit through analysis of whole-rock Sr–Nd isotopes and apatite Sr isotopes. Our results thus allow the source and enrichment mechanism of REEs in the Zhijin phosphorite deposit to be established. The investigation should also provide a reference for the study of REE-associated deposits and the environmental conditions that existed

Table 1
Average chemical composition (wt.%) of the phosphate from Zhijin region.

	Dolomitic phosphorite				Siliceous phosphorite				Phosphoric dolomite			
	Av. (n = 14)	Max.	Min.	Std.	Av. (n = 9)	Max.	Min.	Std.	Av. (n = 7)	Max.	Min.	Std.
SiO_2	2.3	4.4	0.7	1.1	28.8	59.1	12.6	16.1	3.3	9.1	1.0	2.6
Al_2O_3	0.5	0.9	0.1	0.3	4.5	16.3	0.6	4.7	0.5	1.4	0.0	0.5
Fe_2O_3	0.7	1.4	0.3	0.3	3.1	6.8	0.1	2.4	0.8	1.7	0.1	0.6
CaO	47.3	52.9	38.6	5.5	28.5	43.8	2.8	11.6	33.0	37.2	30.0	2.5
MgO	5.0	12.5	0.1	5.0	3.1	8.2	0.3	2.4	17.0	20.8	13.1	3.1
Na_2O	0.1	0.1	0.0	0.0	0.1	0.1	0.0	0.0	0.0	0.0	0.0	0.0
K_2O	0.2	0.3	0.1	0.1	1.3	4.2	0.2	1.2	0.2	0.5	0.0	0.2
MnO	0.0	0.1	0.0	0.0	0.1	0.5	0.0	0.2	0.1	0.2	0.0	0.1
P_2O_5	28.5	37.7	14.6	9.2	17.7	28.2	0.2	8.6	5.9	12.4	0.4	4.4
SO_3	0.2	0.5	0.1	0.1	2.5	12.1	0.1	3.8	0.1	0.5	0.0	0.2
BaO	0.09	0.32	0.02	0.09	0.04	0.07	0.01	0.02	0.05	0.09	0.01	0.04
LOI	12.87	28.84	2.16	10.75	10.61	23.70	4.55	5.27	38.13	44.73	30.24	5.66
Total	99.21	97.09	0.64	100.55	109.65	97.68	3.61	99.10	99.67	98.53	0.38	99.21

during the early Cambrian.

2. Geological SETTING

2.1. Deposit geology

The Zhijin phosphate deposit is located in southwestern China, in the interior of the Yangtze Block and at the southwestern end of the Qianzhong Uplift (Fig. 1; Liu et al., 2016). The orebody has a strip shape in plain view, has an inclination of 10°–15°, extends 20 km in a NE–SW direction, and has a varying width of 0.4–4.0 km (Guo et al., 2017). The average grade of P_2O_5 in the Zhijin phosphate ore is 17.51%, and the grade of rare earth oxides (REO_2) is 0.05%–0.13%. The proven reserves of phosphate ore amount to 1.334 billion tons, with 1.446 million tons of REO_2, of which YO_2 accounts for 32.18% (Liu et al., 2016). The orebody can be divided into four mineralization sections from northeast to southwest: the Jiaguo–Daga, Guohua, Gezhongwu, and Gaoshan sections. The profile of the Gezhongwu mineralization section is well preserved and the orebody there occurs in horizontal bedded or lenticular forms. Clastic phosphorite and fine-grained dolomite are intercalated, and siliceous phosphorite appears at the top in Gezhongwu (Liu et al., 2016). The main exposed strata are the Upper Sinian Dengying, lower Cambrian Gezhongwu, Niutitang, and Mingxinsi formations, together with lower Carboniferous, middle upper Permian, middle Lower Triassic, and Quaternary beds (Fig. 1; Xu et al., 2019).

2.2. Early Cambrian paleogeography

The Precambrian–Cambrian was one of the most significant periods in the history of Earth, as it spanned a time of major changes in the biosphere (e.g., the Cambrian bioexplosion). During this period, so-called phosphorite events occurred in Asia and Australia, characterized by the extensive deposition of phosphorite (with the formation of >100 known phosphorite deposits; Berner et al., 2003; Wen et al., 2011). During the early Cambrian, the first part of the Cambrian life explosion occurred, and abundant shellfish fossils were buried in phosphorite (Zhang et al., 2003; Moysiuk et al., 1989). In southern China, during the Precambrian–Cambrian transition, numerous economic phosphate deposits were formed on the Yangtze platform. From the latest Sinian to the beginning of the Meishucun period of the early Cambrian, the Yangtze platform underwent large-scale transgression, forming a shallow sea. During deposition of the upper Sinian Dengying Formation, a marine transgression occurred, and the ancient land of Guizhou was submerged, initiating the deposition of abundant phosphorites. At the same time, a deep anoxic water mass was brought to the shelf area of the southeast by ocean currents, anoxifying the shelf environment and favoring the deposition of numerous siliceous rocks and shales. During the Qiongzhusi period of the early Cambrian, the large-scale marine transgression of the Yangtze platform ended, sea level lowered, and the Zhijin region was transformed to an inland shelf environment (Wen et al., 2011; Fan et al., 2016).

2.3. Phosphorite

Phosphorus-rich sedimentary rocks with P_2O_5 contents of > 18% are termed as phosphorites. Phosphorite deposits of the Zhijin Region contain phosphatic particles that can be divided into three types depending on their mineral content: dolomitic phosphorite, siliceous phosphorite, and phosphorous dolomite (Table 1, Fig. 2).

In the Zhijin deposit, siliceous phosphorite is distributed mainly in the upper part of the phosphorite series and alternates with dolomitic phosphorite in the lower part. The content of P_2O_5 in siliceous phosphorite is generally 8.2%–28.2% (Fig. 3B) and in dolomitic phosphorite is generally 14.6%–37.7% (Fig. 3A). The phosphorous dolomite is distributed mainly in the lower part of the dolomitic phosphorite (Fig. 3C) and alternates with dolomitic phosphorite in its upper part; the P_2O_5 content in phosphorus dolomite is < 12%, with an average of 5.9%.

The dolomitic phosphorite is gray to gray-black and composed of clastic minerals and dolomite matrix; the clastic materials are mainly phosphate minerals and dolomite (Fig. 3A). The dolomitic phosphorite also contains small amounts of quartz, chalcedony, calcite, and clay minerals, which are scattered in the dolomite matrix in irregular granular form. Phosphate minerals are present as banded, columnar, and granular apatite aggregations, as well as a small number of fossils (<5%, Fig. 3D). The apatite aggregations that we refer to as "francolite grains" are 30–50 μm wide and 180–300 μm long, with directional and semi-directional structures, and are composed of cryptocrystalline nano-apatite, accounting for 85%–90% of the total amount of phosphate minerals. The dolomite matrix also contains phosphate minerals, which we term as "amorphous apatite". These phosphates have no obvious profile and are interwoven with dolomite matrix, and their content is < 5% of the total phosphate.

The siliceous phosphorite is gray to gray-black and has a similar mineral composition to that of the dolomitic phosphorite, but the clastic materials contain more siliceous minerals. The francolite grains are 40–60 μm in width and 150–300 μm in length and account for 80%–85% of the total amount of phosphate minerals. The bioclasts are composed of bacteria, algae, and fossil crustaceans. The interstitial materials are mainly microcrystalline quartz particles and dolomite; amorphous apatite as an interstitial material accounts for 10%–15% of the total amount of phosphate (Fig. 3B, F).

The phosphorus dolomite is gray to gray-white with a small amount of apatite debris, which is composed predominantly of microcrystalline–cryptocrystalline dolomite.

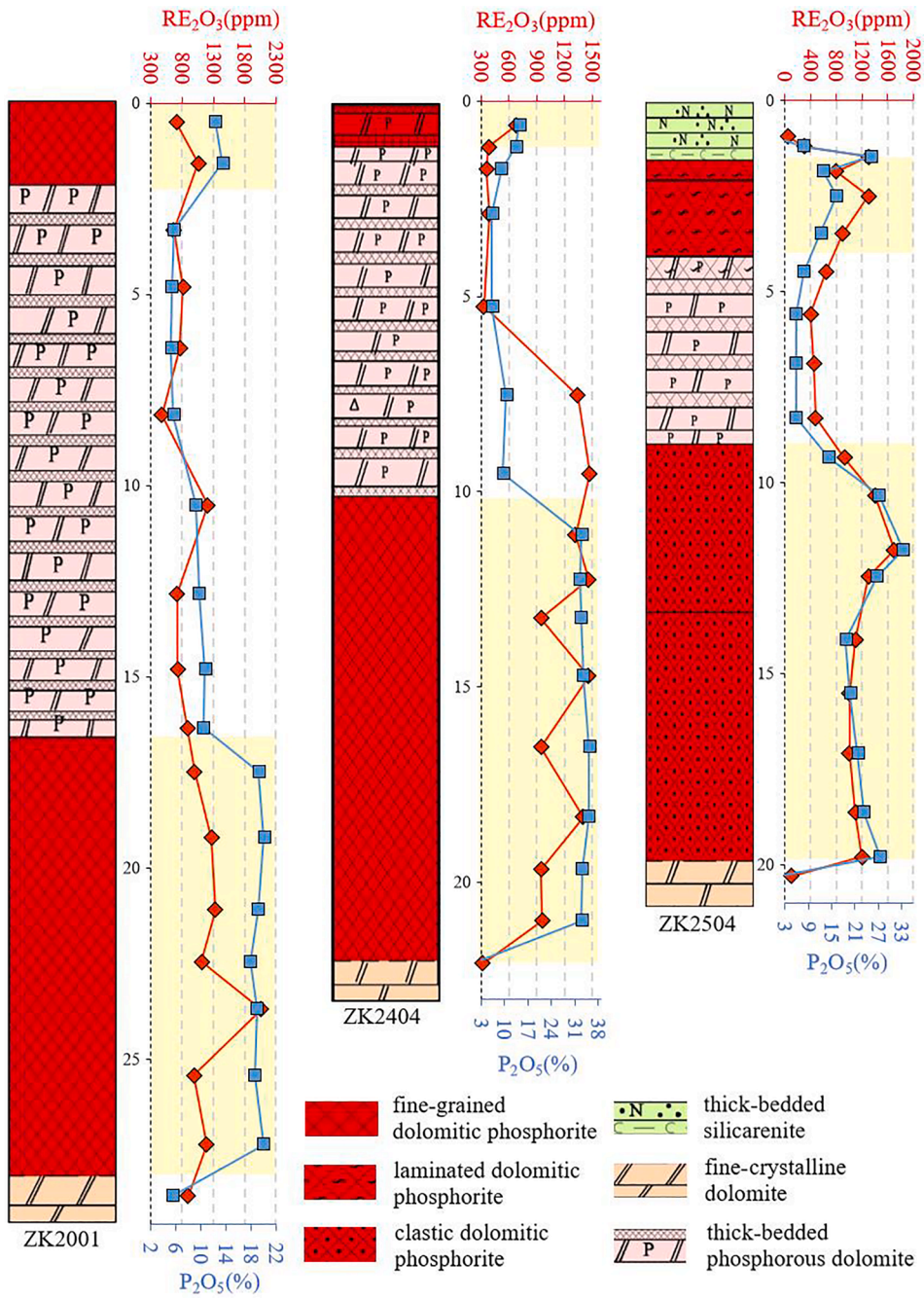

Fig. 2. Drillhole columnar sections of the Zhijin phosphorite deposit.

3. Samples and analytical methods

3.1. Sampling

A total of 64 samples were collected from Linfeichang (LFC), Motianchong (MTC) and Gezhongwu (GZW) in Zhijin region, and 52 polished thin-sections were prepared and examined using both transmitted and reflected light microscopy. 30 fresh rock samples were broken into thumb-sized fragments, then cleaned with 5% dilute hydrochloric acid solution under ultrasonic conditions, then washed with water, dried and removed the contaminated sample fragments visible to the naked eye. Rock fragments were crushed in an agate mortar and ground to <200 mesh powders, which were used for major and trace element and Sr-Nd isotope analysis.

3.2. Transmission electron microscopy (TEM)

TEM study was conducted in the Guangdong Provincial Key Laboratory of Mineral Physics and Materials, Guangzhou Institute of Geochemistry, Chinese Academy of Sciences (GIGCAS). Samples were extracted from thin sections prepared using a special resin, which allows easy extraction of small portions of slices by acetone. After extraction, samples were mounted on copper grids. Ion-beam thinning was performed using a Gatan Duo Million beam thinning machine at 5 kV with a tilt angle of 11. The sample was coated slightly with carbon to prevent charging before TEM analyses. FEI Talos F200S (STEM) was used to take images and perform electron diffraction analysis.

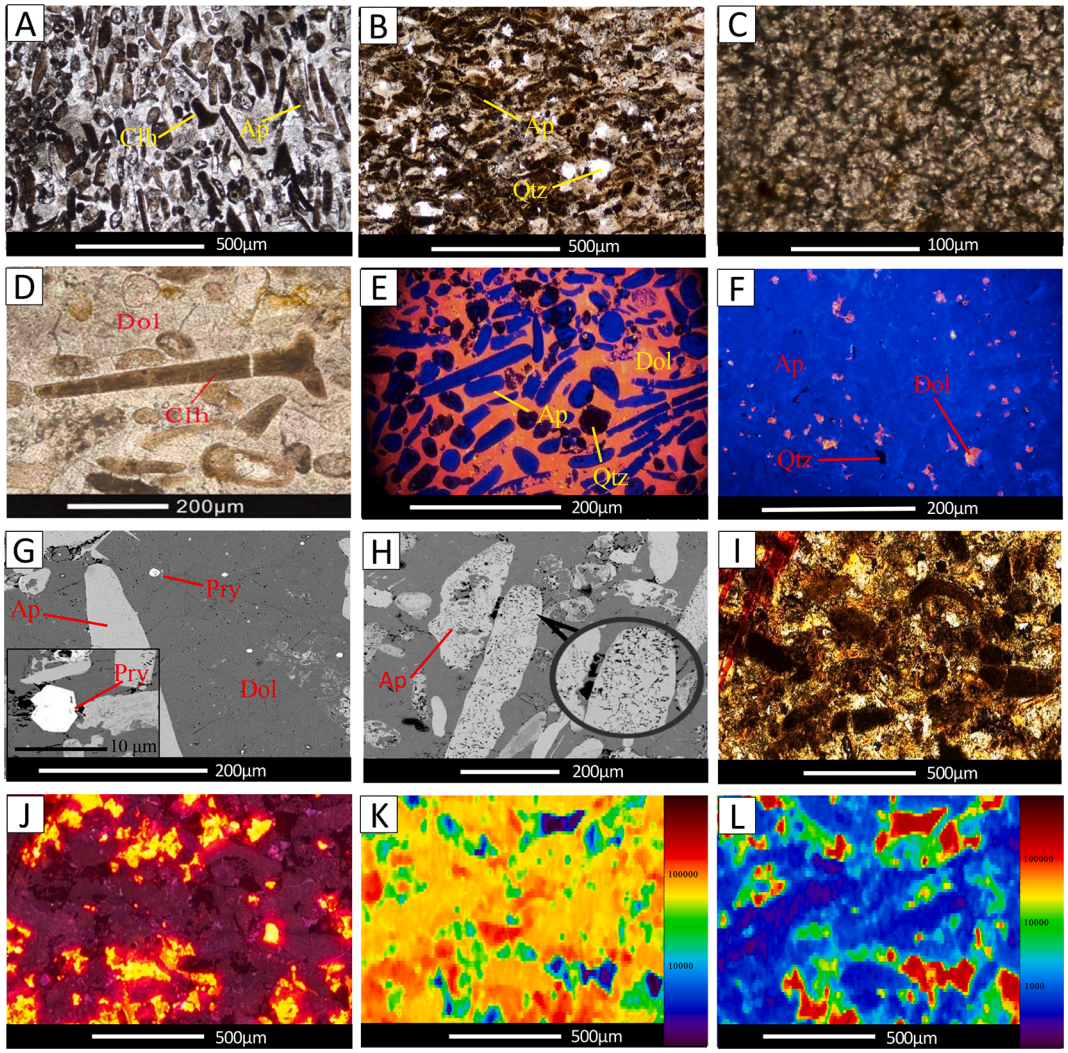

Fig. 3. Microstructural characteristics of phosphorites in the Zhijin region: (A) dolomitic phosphorite; (B) siliceous phosphorite; (C) phosphorous dolomite; (D) bioclasts in phosphorite, after Xu et al. (2019); (E,F) cathodoluminescence image of francolite grains and francolite grains (sapphire colored) mixed with amorphous apatite (orange colored); (G) SEM images of pyrite particles in phosphorite; (H) SEM image of typical francolite grains; (I–L) typical microstructure of sample ZK2002; (J) cathodoluminescence image showing the typical microstructure of sample ZK2002, with francolite grains and amorphous apatite shown in modena color; (K–L) La and Mg (representing dolomite) qualitative elemental maps for sample ZK2002.

3.3. Electron microprobe analysis (EMPA)

EMP analysis was conducted using a JEOL JXA-8100 microprobe at the Guangdong Provincial Key Laboratory of Mineral Physics and Materials, GIGCAS. The analysis was performed using a 15 kV accelerating voltage and a 20nA beam current. The beam spot diameter was set at 1 μm. All data were corrected using standard ZAF correction procedures.

3.4. In situ trace element analysis by LA–ICP–MS

We selected apatite and dolomite from the Zhijin region for in-situ trace element analysis, the analysis was performed using a Resolution M−50 laser ablation system coupled to an Agilent 7500a type ICP-MS at the GIGCAS. Helium was used as a carrier gas to enhance the transport efficiency of the ablated material. Analyses were performed with a beam diameter of 44 μm and a repetition rate of 4 Hz. The counting times were 20 s and 40 s for the background and sample analysis, respectively. A glass standard NIST 610 and NIST 612 was used as an external calibration standard, calcium was used as the internal standard. Precision based on repeated analysis of standards is better than 10%.

3.5. In situ Sr isotope analysis by MC–ICP–MS

In situ Sr isotopic measurements was carried out using a NWR 193 laser-ablation system attached to a Thermo Fisher Scientific Neptune Plus MC-ICP-MS at Beijing Createch Testing Technology Co., Ltd. Instrumental description is given below. A spot size of 60 was employed with a 6–8 Hz repetition rate and an energy density of 10 J/cm^2, depending on the Sr concentration of the samples. Prior to laser analyses, the Neptune MC-ICP-MS was tuned using a standard to obtain maximum sensitivity. A typical data acquisition cycle consisted of a 40 s measurement of the Kr gas blank with the laser switched off, followed by 60 s of measurement with the laser ablating. Every ten sample analyses were followed by one Durango apatite reference material measurement for external calibration.

3.6. Whole-rock Sr–Nd isotopes

Sr was loaded onto tungsten elements with tantalum oxide and analyzed for $^{87}Sr/^{86}Sr$ on a Micromass Sector 54 in dynamic mode at Guizhou Tongwei Analytical Technology Ltd. Two hundred ratios were collected at 1.5 V 88Sr. Mass fractionation was corrected to $^{86}Sr/^{88}Sr =$

Table 2
Trace-element contents (ppm) of phosphate from the Zhijin region.

	Dolomitic phosphorite				Siliceous phosphorite				Phosphoric dolomite			
	Av. (n = 14)	Max.	Min.	Std.	Av. (n = 9)	Max.	Min.	Std.	Av. (n = 7)	Max.	Min.	Std.
Cr	19	40	7.0	7.8	38	110	10	27	14	26	6.0	7.1
Zr	18	28	7.0	7.0	70	178	16	55	8.8	20	2.0	5.7
Co	12	68	0.8	23	5.1	20	1.2	5.4	1.2	2.1	0.8	0.4
Ni	17	75	2.9	26	290	2010	7.2	612	11	41	2.5	13
Th	3.1	4.5	1.6	0.9	7.6	26	2.2	7.0	1.2	2.8	0.06	0.90
U	9.0	21	3.4	4.9	65	309	3.7	103	5.7	15	0.9	5.9
V	12	18	6.0	4.1	90	264	12	97	14	26	6.0	7.1
As	29	151	5.9	41	153	740	3.9	232	7.7	22	0.81	6.8
Sb	17	116	1.6	33	14	52	1.4	15	3.4	5.8	0.85	1.7
Mn	280	808	62	230	697	3510	18	1023	821	1320	186	390
Sr	805	1400	475	255	448	835	88	264	212	361	39	133
La	263	368	141	76.7	156.1	312	36	106.3	62.7	128.0	1.9	46.3
Ce	168	265	86	58.8	154.2	285	69.9	70.5	41.3	77.4	1.8	30.3
Pr	46.0	67.8	25	14.3	34.3	68.2	8.5	18.6	10.8	21.4	0.4	7.9
Nd	197	305	107	64.4	154.1	295.0	32.6	80.7	45.1	89.6	1.6	32.8
Sm	35.4	58.3	19	12.3	30.0	54.1	6.3	14.9	8.0	15.7	0.4	5.8
Eu	9.3	17.2	4.8	3.9	7.9	12.4	1.3	3.6	2.0	3.8	0.1	1.4
Gd	43.8	67.7	24.6	14.4	35.1	65.6	6.0	18.0	10.2	20.3	0.4	7.4
Tb	5.9	8.5	3.4	1.8	4.8	9.2	0.9	2.5	1.4	2.8	0.1	1.0
Dy	35.9	49.5	20.5	10.6	28.2	56.5	5.5	15.8	8.9	17.8	0.4	6.5
Ho	7.6	10.3	4.4	2.2	5.7	11.4	1.1	3.3	1.9	3.9	0.1	1.4
Er	19.7	26.5	11.3	5.6	14.5	29.9	3.2	8.6	5.2	10.0	0.2	3.7
Tm	2.4	3.1	1.4	0.6	1.7	3.6	0.5	1.1	0.6	1.2	0.0	0.4
Yb	11.2	14.8	6.7	2.9	8.3	18.2	3.0	5.1	3.3	6.3	0.2	2.3
Lu	1.5	1.9	0.8	0.4	1.1	2.4	0.4	0.7	0.5	0.9	0.0	0.3
Y	373	522	228	99.7	258.0	493.0	29.0	148.1	96.8	197.0	3.9	70.3

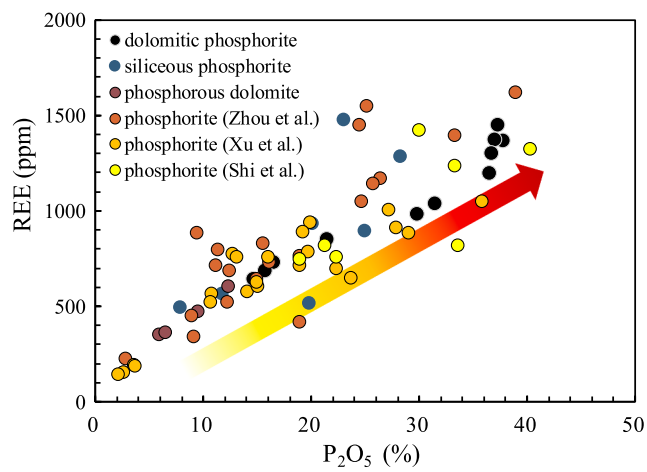

Fig. 4. Compilation of REE contents versus normalized P_2O_5 contents of francolite grains from the Zhijin region.

0.1194. The measured $^{87}Sr/^{86}Sr$ value and the external reproducibility of NIST-987 at the University of Florida is 0.710245 R 0.000023. This external precision is the uncertainty based on replicate analyses of NIST-987 over a period of several years, and it represents the minimum uncertainty assigned to any individual sample, although within-run uncertainties were considerably lower. Twenty replicates analyzed during the study yielded an average difference of 0.000015. Nd concentration data were determined by isotope dilution thermal ionization mass spectrometry. Cleaned, dissolved teeth were spiked for Nd concentrations along with Sr. REEs as a whole were isolated on the first cation exchange column and then processed through an additional cation exchange column using methylacetic acid as an eluent to isolate the Nd and Sm. The total Nd procedural blank is 6 pg. Samples were loaded onto Re elaments with silica gel and analyzed as NdO^+.

4. Results

4.1. Major-element and REE–Y compositions

Major- and trace-element contents of phosphorite from the Zhijin region are given in Tables 1 and 2. The phosphorite can be divided into dolomitic phosphorite, siliceous phosphorite, and phosphorous dolomite, based on differences in element contents. The average P_2O_5 contents of the dolomitic phosphorite, siliceous phosphorite, and phosphorous dolomite are 28.5%, 17.7%, and 5.9%, respectively (Fig. 4). The mean SiO_2 contents are 2.3%, 28.8%, and 3.3%, respectively. The proportionsof francolite grains in phosphorous dolomite are very limited, which can be reflected in the petrographic and geochemical characteristics of dolomite matrix.

The REE–Y compositions of francolite from the Zhijin region (three sampling locations for each phosphorus mine: MTC, LFC, and GZW) were measured by LA–ICP–MS. The total REE–Y contents and elemental ratios are listed in Table 3. The contents are the mean values of several point analyses of each sample and were normalized to Post-Archean Australian shale (PAAS; Taylor and McLennan, 1985; Fig. 5). The total REE contents (ΣREE) of the francolite range from 778 to 1451 ppm, with means values of 1047 ppm for the LFC, 1160 ppm for the MTC, and 865 ppm for the GZW. The Y contents of the francolite range from 363 to 664 ppm, with means values of 502 ppm for the LFC, 536 ppm for the MTC, and 416 ppm for the GZW.

Anomalies of Ce/Ce*, Pr/Pr*, and Eu/Eu* were calculated after Bau and Dulski (1996):

$Ce/Ce^* = (Ce_{sample}/Ce_{shale})/[0.5*(La_{sample}/La_{shale}) + 0.5*(Pr_{sample}/Pr_{shale})]$,

$Pr/Pr^* = (Pr_{sample}/Pr_{shale})/[0.5*(Ce_{sample}/Ce_{shale}) + 0.5*(Nd_{sample}/Nd_{shale})]$,

and

$Eu/Eu^* = (Eu_{sample}/Eu_{shale})[0.5*(Sm_{sample}/Sm_{shale}) + 0.5*(Gd_{sample}/Gd_{shale})]$.

All samples have pronounced negative Ce/Ce* anomalies (0.30–0.42) and weak positive Pr/Pr* anomalies (1.07–1.23). Eu/Eu* anomalies are mainly weak negative or absent (0.88–1.04), although some samples from the LFC (with higher SiO_2 content) show pronounced

Table 3
Contents of REEs (in ppm) in phosphate from the Zhijin region, after Zhang et al. (2007).

	Sample	La	Ce	Pr	Nd	Sm	Eu	Gd	Tb	Dy	Ho	Er	Tm	Yb	Lu	Y	ΣREE	Ce/Ce*	Eu/Eu*	Pr/Pr*	LaN/SmN	LaN/YbN
LFC	LFC-3–2	372.09	188.24	51.92	236.21	41.71	8.95	52.59	6.57	41.92	9.43	22.82	2.80	14.30	1.79	504.96	1051.33	0.31	0.88	1.14	1.67	2.45
	LFC-3–7	353.51	191.89	55.73	260.85	45.94	9.82	54.57	7.29	44.61	9.48	23.23	2.42	12.66	1.46	501.87	1073.46	0.32	0.91	1.12	1.44	2.63
	lfc-2–1	377.27	194.43	55.95	244.98	43.17	9.28	54.65	7.34	44.16	9.60	24.08	2.65	13.76	1.65	512.58	1082.97	0.31	0.88	1.18	1.64	2.59
	lfc-2–6	416.04	214.79	60.63	273.78	49.22	10.74	60.07	7.99	48.56	10.37	26.18	2.90	14.74	1.79	547.76	1197.79	0.31	0.92	1.15	1.58	2.66
	lfc-2–11	387.29	201.74	55.53	252.85	45.68	9.80	54.76	7.54	45.66	9.87	24.56	2.78	13.37	1.73	535.52	1113.15	0.31	0.91	1.13	1.59	2.73
	lfc-2–14	258.19	152.24	47.06	218.50	43.64	10.27	49.84	6.46	39.86	8.41	20.30	2.09	10.81	1.18	430.08	868.86	0.32	1.03	1.15	1.11	2.25
	lfc-2–19	355.04	180.09	50.76	222.97	39.23	9.40	50.60	6.86	43.39	9.05	22.21	2.50	13.51	1.48	499.31	1007.10	0.31	0.97	1.17	1.70	2.48
	lfc-2–23	369.15	178.05	46.82	207.14	36.08	7.73	44.89	6.27	39.17	8.55	22.39	2.66	13.49	1.70	488.51	984.10	0.30	0.89	1.15	1.92	2.58
MTC	MTC-1–1	393.66	220.28	62.83	281.46	51.93	11.76	62.62	8.22	49.00	10.41	25.49	2.95	13.74	1.78	557.36	1196.13	0.32	0.96	1.16	1.42	2.70
	MTC-1–6	413.33	226.74	63.67	263.01	46.73	10.73	55.18	7.19	45.65	9.94	24.01	2.87	13.30	1.82	516.24	1184.18	0.32	0.98	1.23	1.66	2.93
	MTC-1–15	403.36	225.41	62.60	282.21	52.48	11.17	60.69	8.49	50.30	10.65	26.88	3.00	14.88	1.87	563.07	1213.99	0.33	0.92	1.14	1.44	2.56
	MTC-1–18	351.68	235.41	75.15	358.90	64.06	13.84	71.05	8.97	53.66	10.65	23.84	2.36	10.14	1.04	508.46	1280.76	0.34	0.96	1.13	1.03	3.27
	MTC-1–23	522.85	270.70	73.82	322.97	54.97	11.60	66.35	8.77	55.35	11.79	29.77	3.44	17.18	2.20	644.97	1451.77	0.31	0.89	1.17	1.78	2.87
	MTC-3–1	395.88	199.15	55.27	244.84	42.89	9.32	53.60	7.22	43.77	9.57	24.82	2.87	15.14	1.95	539.09	1106.29	0.31	0.90	1.16	1.73	2.47
	MTC-3–6	399.74	203.67	57.75	259.94	45.20	10.31	56.02	7.54	45.86	10.29	25.25	2.94	15.05	1.81	551.34	1141.36	0.31	0.95	1.15	1.66	2.50
	MTC-3–14	367.49	180.31	48.70	216.81	38.42	8.50	47.46	6.48	39.00	8.56	21.96	2.73	13.65	1.69	496.60	1001.75	0.30	0.92	1.15	1.79	2.54
	MTC-3–20	295.76	152.95	43.60	195.33	36.90	8.08	44.80	5.97	36.86	7.95	20.17	2.25	12.05	1.54	451.10	864.22	0.31	0.92	1.16	1.50	2.31
GZW	ZK2504-6	281.00	144.71	40.89	182.26	34.67	7.46	41.29	5.62	34.77	7.62	19.77	2.26	11.28	1.49	423.09	815.08	0.31	0.91	1.16	1.52	2.35
	ZK2504-9	347.77	178.26	49.13	209.99	37.42	7.92	45.63	6.10	38.34	8.72	22.07	2.51	13.54	1.70	472.27	969.09	0.31	0.89	1.19	1.74	2.42
	ZK2504-14	379.49	193.69	54.68	242.25	43.14	8.92	53.46	7.17	45.18	9.46	24.22	2.76	14.92	1.77	521.11	1081.09	0.31	0.86	1.16	1.65	2.40
	ZK2504-22	341.37	177.07	48.53	212.51	37.60	8.35	46.65	6.26	38.65	8.53	21.44	2.48	12.61	1.52	462.53	963.58	0.31	0.92	1.17	1.70	2.55
	ZK2504-31	300.76	148.04	39.93	179.82	31.21	6.62	39.80	5.38	35.68	7.86	20.57	2.49	12.15	1.51	436.59	831.82	0.30	0.87	1.14	1.81	2.33
	ZK2004-01	256.75	139.91	40.41	186.38	35.43	8.31	42.60	5.84	35.96	7.84	19.16	2.18	10.43	1.28	408.44	792.49	0.32	0.99	1.14	1.36	2.32
	ZK2004-05	320.16	165.84	46.13	206.33	36.94	7.98	46.26	5.87	37.46	8.41	21.27	2.43	12.38	1.49	444.89	918.96	0.31	0.89	1.15	1.62	2.44
	ZK2004-11	288.67	145.09	37.53	167.23	28.14	6.03	35.68	4.92	30.12	6.70	18.26	2.19	10.63	1.41	389.20	782.59	0.31	0.88	1.13	1.92	2.56
	ZK2004-20	311.84	155.78	41.88	187.29	33.69	6.88	39.63	5.62	34.86	7.65	19.80	2.41	12.64	1.60	426.77	861.58	0.31	0.87	1.14	1.73	2.33
	ZK2002-8	296.79	219.33	48.29	219.90	42.47	10.13	48.64	6.74	40.89	8.85	21.27	2.44	11.73	1.59	403.94	979.06	0.42	1.04	1.07	1.31	2.39
	ZK2002-23	250.10	191.18	45.03	216.02	41.88	9.40	50.00	6.64	38.33	7.99	19.27	2.10	10.30	1.21	363.60	889.45	0.42	0.95	1.05	1.12	2.29
Bioclast	1	117.53	75.64	17.93	78.6	13.86	3.21	16.49	2.31	14.31	3.08	8.48	1.02	5.29	0.72							
	2	113.72	66.59	18.32	80.23	13.95	3.26	16.51	2.36	14.75	2.97	8.17	0.99	4.99	0.69							
Shelly fossil	1	28.3	35.7	7.47	36.2	8.58	2.58	13.4	1.75	10.2	2.17	5.4	0.89	3.1	0.65							
	2	41.1	58.3	11.5	55.9	15.2	3.68	17.1	2.53	15.2	3	7.76	1.22	4.72	0.96							
Dolomite	1	10.7	18.7	2.53	10.5	2.08	0.44	2.36	0.34	1.95	0.39	1.08	0.15	0.83	0.13							
	2	1.6	1.7	0.25	1.1	0.2	0.07	0.26	0.03	0.17	0.04	0.11	0.01	0.07	0.01							

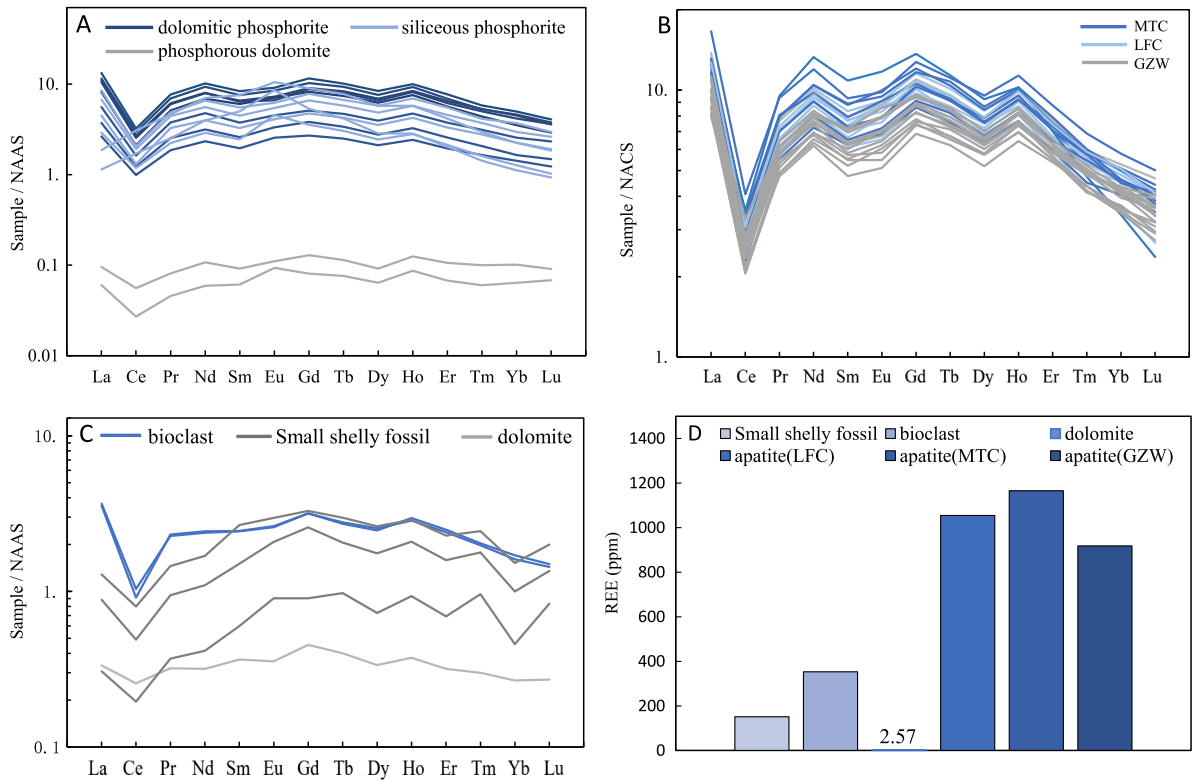

Fig. 5. Post-Archean Australian shale (PAAS; Taylor and McLennan, 1985) normalized REY patterns of representative phosphorite samples. (A) REEs of the whole rock, dolomitic phosphorite, siliceous phosphorite, and phosphorous dolomite. (B) REEs of francolite grains of the MTC, LFC, and GZW. (C) REEs of small shelly fossils, bioclasts, and dolomite, after Zhang et al. (2007). (D) REE contents in various minerals, after Zhang et al. (2007).

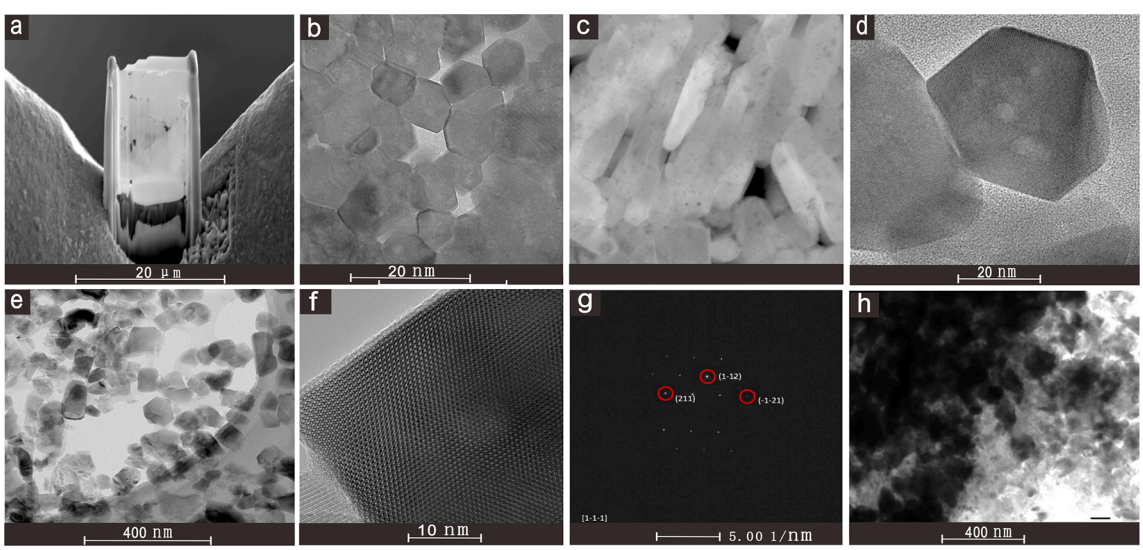

Fig. 6. Bright-field TEM images of apatites in francolite grains of siliceous phosphorite in Zhijin. (a) SEM image of an FIB slice of a typical francolite grain. (b–e) Enlargement of the image in (a), showing hexagonal hydroxyapatite nano-crystals observed in the direction of the c-axis. (f–g) HRTEM image of a nano-crystal with its FFT pattern indicating a zone axis orientation of [0 0 1]. (h) Bright-field TEM image of typical amorphous apatite, after Liu (2008).

positive anomalies. Compared with LREEs and HREEs, MREEs show slight enrichment. Relative to modern seawater (Reynard et al., 1999), the high $(La/Yb)_N$ ratios of francolite grains imply that they are enriched in LREEs, which may be related to the abnormally high La content. However, values of $(La/Sm)_N$ are in the range of modern seawater.

It should be noted that LA–ICP–MS analyses carefully avoided ablation of non-apatite minerals and that abundant data were analyzed, but francolite from Zhijin is composed of aggregates of numerous microcrystalline individual apatite grains, meaning that there may be a small amount of matrix (dolomitic or siliceous) in spaces between mineral aggregates, resulting in some non-apatite minerals being ablated. However, whole-rock trace-element analyses of REE contents and REE partitioning in the phosphorite are similar to those of francolite grains, meaning that any interference of the phosphorite matrix was negligible.

Table 4
Sr-Nd isotopic compositions of the phosphate and carbonate fractions in the rock samples.

	dolomitic phosphorite		siliceous phosphorite			phosphoric dolomite						
	Av.(n=14)	Max.	Min.	Std.	Av.(n=9)	Max.	Min.	Std.	Av.(n=7)	Max.	Min.	Std.
SiO_2	2.3	4.4	0.7	1.1	28.8	59.1	12.6	16.1	3.3	9.1	1.0	2.6
Al_2O_3	0.5	0.9	0.1	0.3	4.5	16.3	0.6	4.7	0.5	1.4	0.0	0.5
Fe_2O_3	0.7	1.4	0.3	0.3	3.1	6.8	0.1	2.4	0.8	1.7	0.1	0.6
CaO	47.3	52.9	38.6	5.5	28.5	43.8	2.8	11.6	33.0	37.2	30.0	2.5
MgO	5.0	12.5	0.1	5.0	3.1	8.2	0.3	2.4	17.0	20.8	13.1	3.1
Na_2O	0.1	0.1	0.0	0.0	0.1	0.1	0.0	0.0	0.0	0.0	0.0	0.0
K_2O	0.2	0.3	0.1	0.1	1.3	4.2	0.2	1.2	0.2	0.5	0.0	0.2
MnO	0.0	0.1	0.0	0.0	0.1	0.5	0.0	0.2	0.1	0.2	0.0	0.1
P_2O_5	28.5	37.7	14.6	9.2	17.7	28.2	0.2	8.6	5.9	12.4	0.4	4.4
SO_3	0.2	0.5	0.1	0.1	2.5	12.1	0.1	3.8	0.1	0.5	0.0	0.2
BaO	0.09	0.32	0.02	0.09	0.04	0.07	0.01	0.02	0.05	0.09	0.01	0.04
LOI	12.87	28.84	2.16	10.75	10.61	23.70	4.55	5.27	38.13	44.73	30.24	5.66
Total	99.21	97.09	0.64	100.55	109.65	97.68	3.61	99.10	99.67	98.53	0.38	99.21

4.2. Micro-petrography and mineralogy

Individual crystals of apatite can be observed clearly using TEM. At × 100,000 magnification, francolite is observed to consist of pure apatite crystals, with the electron diffraction pattern showing the characteristics of apatite (Fig. 6). Individual apatites are pseudohexagonal granular or short columnar, with a self-shaped structure. Short axes measure 40–100 nm, with most 50–70 nm, and long axes are 80–250 nm, with most 120–160 nm. Individual crystal particles adsorb each other and form granular francolite grains. Under TEM, grain boundaries of apatite are regular and clear without connected crystals or growth edges. These nanometer-sized apatites have a chemical origin, with no biological residue or biological structure.

Studies of crystal morphology have shown that the growth and evolution of individual crystals in polycrystalline aggregates are not irregular but coordinated with each other (e.g., Zhao, 2016). In the francolite of the Zhijin phosphorite, individual apatite crystals do not restrict each other but grow together harmoniously (Fig. 6b,c). We infer that the apatite crystals have a simple relationship of mutual adhesion. The crystals were connected by physical adsorption on surfaces and were then deformed during mineralization (Fig. 6d,e).

In the Zhijin region, amorphous apatite in the form of cement is

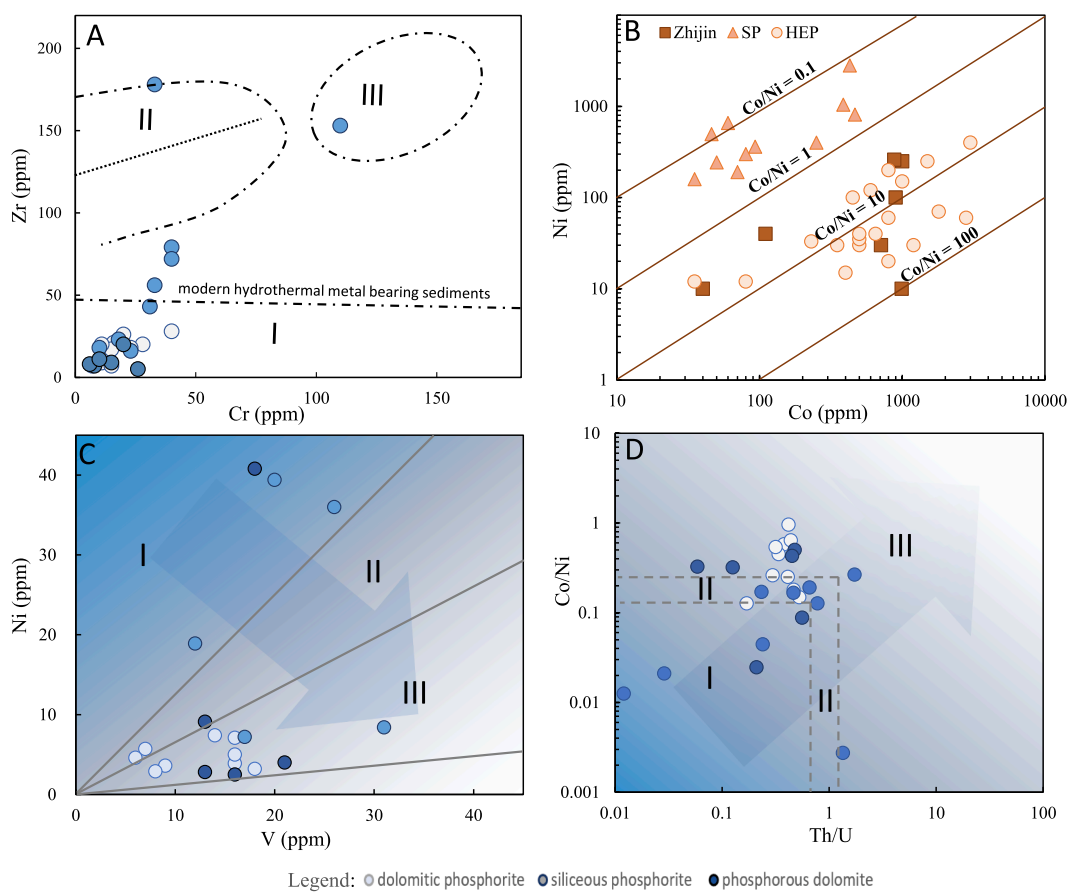

Fig. 7. Plots of sedimentary environment parameters for phosphorite samples from Zhijin. (A) Zr–Cr diagram showing data for different phosphorites, after Marchig (1982). I: Seawater hydrothermal trend line, II: hydrogenic sediment field, III: hydrodiagenetic-metal-bearing sediment field. (B) Ni–Co diagram for pyrite, after Huston et al. (1995), Large et al. (2007) and Zhao (2016). Abbreviations: SP: sedimentary pyrite, HEP: hydrothermal exhalation pyrite. (C–D) Diagrams of oxidation–deoxidation environment parameters of phosphorite samples from Zhijin, after Ross and Bustin (2006). legend: I: oxidation environment, II: suboxidation environment, III: reduction environment.

distributed in the matrix of dolomitic phosphorite and siliceous phosphorite. Electron microprobe analysis showed that the amorphous apatite was composed mainly of apatite minerals and minor bio-organic residues (Fig. 6h). This type of apatite accounts for only 5%–10% of the total and was therefore not investigated further in this study.

4.3. Sr-Nd isotope measurements

Isotopic ratios of Sr and Nd are listed in Table 4, including whole-rock Sr and Nd ratios, as well as Sr ratios of individual minerals. The Nd content of francolite grains is < 400 ppm, which does not allow accurate estimates to be made of in situ Nd isotope ratios. Initial $^{143}Nd/^{144}Nd$ ratios of the phosphorites range from 0.511944 to 0.512074, and εNd (543 Ma) values vary from − 7.18 to − 5.65.

Ratios of $^{87}Sr/^{86}Sr$ of phosphorite in the samples are 0.708716–0.710231, except for LFC-3–4, which has a ratio of 0.713129. Initial (543 Ma) $^{87}Sr/^{86}Sr$ ratios of the whole rock and in situ francolite grains are 0.707904–0.709095 and 0.708701–0.709399, respectively.

5. Discussion

5.1. Paleosedimentary environment of phosphorite

5.1.1. Hydrothermal–sedimentary system

If a hydrothermal system injects fluid into the sea or a lake basin, then sedimentation is controlled and induced by the hydrothermal medium (e.g., seawater, lake water, hot spring, with a water temperature of 70–350 °C); the system is thus referred to as hydrothermal–sedimentary, and the deposit formed is termed as a hydrothermal–sedimentary deposit (Chen et al., 1992; Zhao, 2016). During hydrothermal processes, Cr is partly mobile and is enriched in hydrothermal precipitates without being followed by other lithophile element (Marchig, 1982). Consequently, the correlation between Cr and Zr decreases during hydrothermal sedimentary and can be negligible. However, the Cr/Zr ratio in diagenetic metalliferous sediments is similar to that in deep-sea sediments, and the correlation between Cr and Zr is high. The Zr contents in hydrothermal metalliferous sediments is generally < 50 ppm and does not increase with increasing Cr contents (Marchig, 1982). In contrast, Zr contents in deep-sea sediments and diagenetic metalliferous sediments usually exceed 100 ppm. The Zr contents in the dolomitic phosphorites, siliceous phosphorites, and phosphorous dolomites from Zhijin are 7.0–28 ppm, 16–178 ppm (mostly < 40 ppm), and 2.0–20 ppm, respectively (Fig. 7A, Table 3). Data for the three types of phosphorite sample fall near the line of modern hydrothermal-metal-bearing sediments, suggesting a hydrothermal–sedimentary origin.

Pyrite (FeS_2) can contain up to 50 trace elements, which can provide important geochemical information, such as the origin and genesis of the deposit (Thomas et al., 2011). Pyrite with high degrees of automorphism is widely distributed in the dolomite matrix of the Zhijin phosphorite samples (Fig. 3G). A total of 22 morphologically regular pyrites from the phosphorite samples were analyzed for trace-element contents. The pyrites are tiny and isolated, scattered, and embedded in the matrix, and show no relationship with francolite. The Co contents in these pyrites are 10–1100 ppm, with a mean of 749 ppm. The Ni contents in 14 pyrite grains are lower than the detection limit, and the Ni contents in 8 pyrite grains range from 10 to 260 ppm. The most significant feature of pyrite is that Co and Ni replace Fe^{2+}, which changes the cell parameters of pyrite (Dill and Kemper, 1990; Guy et al., 2010). In hydrothermal–sedimentary deposits, Co preferentially enters the pyrite lattice due to its lower unit cell coefficient and becomes enriched in pyrite with Co/Ni > 1, whereas in low-temperature sedimentary deposits, Ni can enter the pyrite lattice more easily than Co, with Co/Ni < 1 (Bajwah et al., 1987; Dill and Kemper, 1990; Guy et al., 2010; Gregory et al., 2015; Zhao 2016). With a mean value of 10 for Co/Ni (Fig. 7B), the Zhijin pyrite is interpreted to have formed in a hydrothermal–sedimentary environment.

Previous geochemical and petrographic investigations have also revealed that phosphorites from the Zhijin region show the characteristics of hydrothermal sediments (Shi, 2005; Chen et al., 2006; Quan et al., 2007; Jia et al., 2018; Liu et al., 2019; Zhang et al., 2019; Qiu et al., 2021). Shi (2005) pointed out that As and Sb in phosphorite are enriched relative to the average sedimentary rock content for Zhijin and that the phosphorite shows hydrothermal–sedimentary features (Boström, 1983; Marchig, 1982). Our samples show these same characteristics. An Fe–Al–Mn diagram for Zhijin phosphorite also suggests that the deposition of phosphorite was influenced by hydrothermal sedimentation (Quan et al., 2007). Furthermore, Liu et al. (2019) identified isolated primary fluid inclusions in siliceous phosphorite of the GZW and in dolomitic phosphorite of the Guohua ore-section, for which the homogenization temperature was estimated as 87.5–184.3 °C, implying that the original hydrothermal fluid was low temperature.

5.1.2. Anoxic environment

Study of the oxidation–reduction environment of sedimentary deposits can give insights into the sedimentary depositional environment and genesis. Elements such as V, Ni, Co, Th, and U in sediments are redox sensitive (Francois, 1988; Anderson et al., 1989; Ross and Bustin, 2006; Wei, 2012), and the ratios of these elements can be used as indicators to estimate the bottom-water environment of sediments. The ratios of V/Ni, Co/Ni, and Th/U are often used as indicators to determine the redox state of paleo-marine environments (Jones and Manning, 1994; Wignall and Twitchett, 1996).

Compared with Ni, V tends to be enriched in anoxic environments, with high V/Ni ratios indicating a reductive anoxic sedimentary environment. The V and Ni contents in the Zhijin phosphorite are 4.1–264 ppm and 2.5–40.8 ppm, respectively (Table 3). The aqueous environment can be divided into four types based on V/Ni ratios: oxidation environment < 0.8, lean oxygen environment 0.8–1.5, anoxic environment 1.5–6, and sulfide environment > 6 (Lewan and Maynard, 1982; Lewan, 1984; Hatch and Leventhal, 1992). In Fig. 7C, most phosphorite data fall in Region III, representing an anoxic environment, with a few data for siliceous phosphorite falling in Region I, representing an oxidation environment, which may be related to the material source of silicon.

The migration of Th is restricted in low-temperature surface environments, and its content is enriched in weathering-resistant minerals, whereas U can be readily precipitated in the tetravalent state in reducing environments. Therefore, the Th/U ratio can reflect the redox condition of water and is a commonly used indicator of redox condition in sedimentary environments (Adams and Weaver, 1958; Kimura and Watanabe, 2001; Wei, 2012). The Th/U ratios of dolomitic phosphorites, siliceous phosphorites, and phosphorous dolomites are 0.17–0.52, 0.03–1.73, and 0.06–0.56, respectively (Fig. 7D). The study of Jones and Manning (1994) proposed that Th/U > 1.33 indicates an oxidizing aqueous environment, Th/U = 0.8–1.33 indicates an oxygen-poor aqueous environment, and Th/U < 0.8 indicates an anoxic aqueous environment.

Ratios of Co/Ni have been used to infer bottom-water conditions during sedimentation (Jones and Manning, 1994; Rimmer, 2004; Ross and Bustin, 2006). The Co contents in the studied dolomitic phosphorites, siliceous phosphorites, and phosphorous dolomites are 0.8–68 ppm, 1.2–20 ppm, and 0.8–2.1 ppm, respectively (Table 3). Lower Co/Ni ratios are associated with decreasing oxygen content during deposition (Jones and Manning, 1994), owing to the relatively easy isolation of Ni from organic matter in reduced sediments (Breit and Vanty, 1991). However, Co content a function of detrital content and is not affected by redox conditions (Dill, 1986; Ross and Bustin, 2006). The Co/Ni ratios respectively are 0.08–2.27, 0.02–0.27 and 0.02–0.43 of Zhijin dolomitic phosphorites, siliceous phosphorites, and phosphorous dolomites (Fig. 7D). Jones and Manning (1994) compared Co/Ni values with the DOP value and proposed that a value of Co/Ni of > 0.2 indicates an

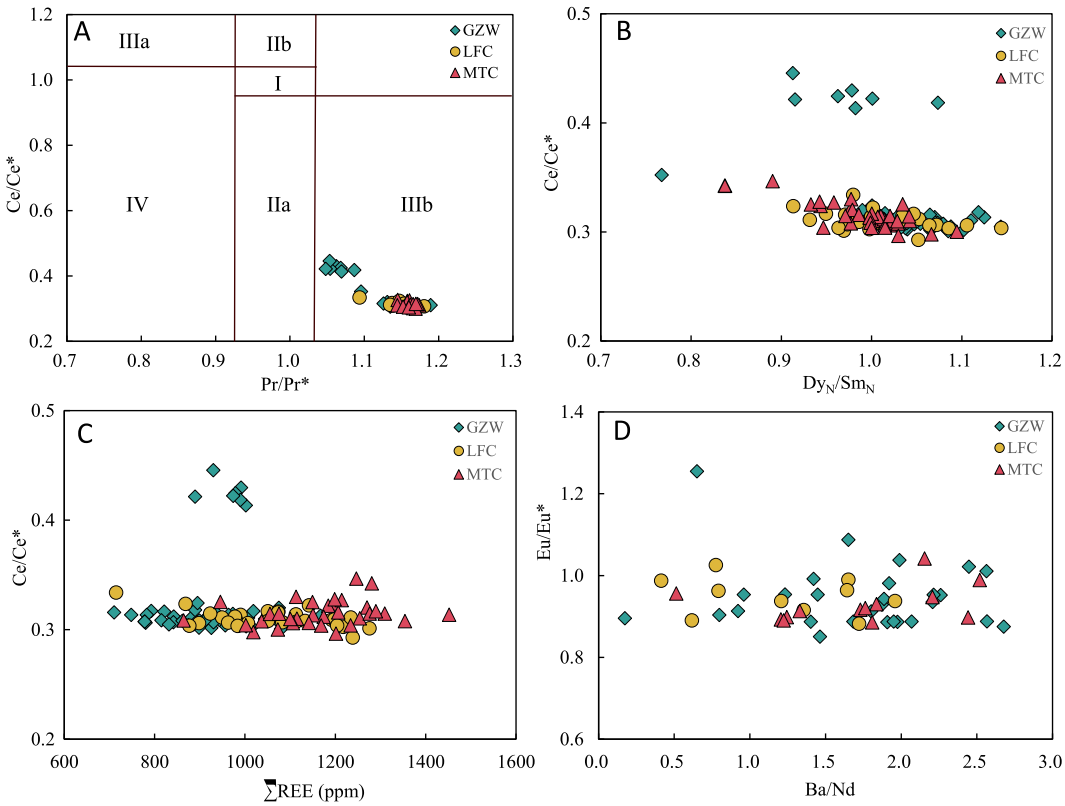

Fig. 8. Plots of Ce and Eu anomalies plotted against various other REE parameters for francolite grains from Zhijin. (A) Ce/Ce* vs. Pr/Pr* diagram, after Bau and Dulski (1996); Field I: no anomaly, Field IIa: positive La anomaly causing an apparent negative Ce anomaly, Field IIb: negative La anomaly causing an apparent positive Ce anomaly, Field IIIa: true positive Ce anomaly, Field IIIb: true negative Ce anomaly, Field IV: positive La anomaly disguising a positive Ce anomaly. (B–C) Ce/Ce* versus other REE parameters, after Xin et al. (2015); (D) Eu/Eu* vs. Ba/Nd, after Ling et al. (2013).

oxidation environment and that a value of < 0.14 indicates an anoxic environment.

In a Th/U–Co/Ni diagram (Fig. 7D), most data for the siliceous phosphorites and dolomite phosphorites fall in the anoxic or lean oxygen areas, indicating an anoxic reduction paleosedimentary environment, and especially the phosphorous dolomite can better reflect the sedimentary environment of dolomite matrix in phosphorite. However, most data for the dolomite phosphorites plot in the oxidation environment area, which may reflect the presence of francolite grains derived from distant sources.

5.2. Diagenetic processes of francolite grains

5.2.1. Redox proxies: Ce/Ce* and Eu/Eu*

REE geochemical characteristics can constrain the nature of the sedimentary and diagenetic environment, especially the REE sources of marine sediments of phosphorites (Marchig, 1982; Grandjean et al., 1988; German and Elderfield, 1990; Bertram et al., 1992; Jarvis et al., 1994; Reynard et al.,1999; Hannigan and Sholkovitz, 2001; Shields and Stille, 2001; Picard et al., 2002; Qiu et al., 2019; Wu et al., 2021). The REEs contents in the studied francolite grains can be used to reveal the redox environment of the host sediments, especially the elements Ce and Eu.

A plot of Ce/Ce* versus Pr/Pr* can be used to characterize redox conditions using PAAS-normalized REE contents (Table 3; Fig. 8A). The plot also allows evaluation of the Ce anomaly with respect to possible spurious results caused by anomalous enrichment of La (Bau and Dulski, 1996; Shields and Stille, 2001; Garnit et al., 2012). Ce/Ce* records true anomalies (Fig. 8A, Field IIIB), excess Ce relative to adjacent lanthanides (Fig. 8A, Field IIIA), or Ce/Ce* related to insufficient abundance of La (Fig. 8A, Field IIB; Bau and Dulski, 1996). Our data are concentrated in the IIIB region (Fig. 8A), indicating that they represent true negative Ce anomalies that are unrelated to La abundance.

Cerium anomalies in seawater are controlled mainly by redox conditions, meaning that they can be used as tracers of redox conditions (German and Elderfield, 1990; Jiang et al., 2007; Zhu et al., 2014; Xin et al., 2015). In the studied Zhijin francolite grains, Ce/Ce* values for the GZW, LFC, and MTC are 0.31–0.45, 0.31–0.33, and 0.30–0.33, respectively (Table 3). In oxygen-containing marine environments, Ce^{4+} is dominant and is removed by highly reactive Fe–Mn–oxyhydroxides, resulting in the depletion of Ce in oxygen-containing seawater (Elderfield and Greaves, 1982). In anoxic environments, Ce behaves similarly to other trivalent REEs. Water depth, pH, and brine age also affect Ce anomalies to some extent (German and Elderfield, 1990; Xin et al., 2015). According to Shields and Stille (2001), REE enrichment and values of $(Dy/Sm)_N$ decrease during diagenesis. Ce/Ce* is negatively correlated with the $(Dy/Sm)_N$ ratio, and Ce/Ce* is positively correlated with ΣREE content. However, our data show no obvious variation in the Ce anomaly and no obvious correlations with other geochemical indicators (Fig. 8B,C), which suggests that there was no obvious change in the Ce anomaly during diagenetic processes and that francolite grains were unaffected by diagenetic alteration. The Ce/Ce* ratio is usually used as a proxy for inferring redox conditions during the deposition of authigenic minerals such as francolite (Wright et al., 1987), and the negative Ce anomalies of our samples suggest that the Zhijin francolite was formed in an oxidizing, rather than anaerobic, environment.

Values of Eu/Eu* for samples from the GZW, LFC, and MTC are 0.87–1.25, 0.88–1.02, and 0.89–1.04, respectively (Table 3). However, Ba contents in the Zhijin samples are high (mostly > 200 ppm), as a result of the interference of Ba on Eu during ICP–MS analyses (Dulski, 1994), with high Ba contents affecting Eu contents and anomalies. Such an effect can be detected by a positive correlation between Eu/Eu* and

Ba/Nd (Ling et al., 2013). As shown in Fig. 8D, there is no correlation between Eu/Eu* and Ba/Nd in the francolite grains, meaning that the determined Eu anomalies are reliable. The valence state of Eu is different from the strictly trivalent state of other REEs, as it contains both divalent and trivalent ions, with the relative abundance of Eu^{2+} and Eu^{3+} being controlled by redox conditions, pH, and temperature (De Baar et al., 1985; Gadd et al., 2016). Eu^{2+} is the common form under reducing conditions, alkaline environment, or high temperature (>250 °C), and migrates to phosphate, resulting in positive Eu anomalies (Sverjensky, 1984). In addition to a reducing environment, submarine hydrothermal fluid can also cause positive Eu anomalies (Stalder and Rozendaal, 2004; Pi et al., 2013). In low-temperature environments (about 25 °C), Eu is dominated by its trivalent state (Sverjensky, 1984). However, although we have confirmed that the Eu anomalies determined in this study are reliable, unambiguous inference of the redox environment cannot be made because of the various factors influencing these anomalies.

5.2.2. Possible transportation of francolite grains

The Zhijin phosphorite was deposited in a coastal environment between continent and islands. This environment was influenced by marine transgression and to the cyclic action of ocean currents, storms, tides, and waves, which generated strong hydrodynamic effects (Zhang et al., 2007a; Zhang et al., 2007b; Liu et al., 2016). The paleoenvironment of the Zhijin phosphorite was a high-energy environment, and the early phosphate was accumulated, eroded, and transported by strong hydrodynamic action (Yang and He, 2013; Liu et al., 2016). This hypothesized environment of deposition is supported by our geochemical analyses and visual inspection of BSE micrographs. Our geochemical analyses indicate that the diagenetic environment of the francolite grains was oxidic, whereas the sedimentary environment of the phosphorite was anoxic, and the differences in their geochemical characteristics well reflect the allopatric diagenetic peculiarity of these apatite clasts. The francolite grains are homogeneous and bright under BSE imaging (Fig. 3H). However, in each francolite grain, fractures can be observed under BSE imaging. These fractures are filled by dolomitic matrix or are hollow (Fig. 3H), and some contain sporadic dark-gray granular quartz measuring 3–5 μm. These fractures were likely caused by abrasion and transportation of the francolite grains, suggesting that these grains might have been exposed in seawater and transported for a prolonged period (Auer et al., 2017).

5.3. Enrichment of REEs in francolite grains

5.3.1. Occurrence of REEs

It is generally accepted that phosphatic sediments contain higher REE and Y contents compared with other sedimentary rocks (Jarvis et al., 1994; Kidder et al., 2003). These elevated contents are due to the substitution of Ca^{2+} by REE^{3+} and Y^{3+} in apatite and the adsorption process of REEs by mineral particles (Webb and Kamber, 2000; Shields and Webb, 2004; Zhao et al., 2013; Chen et al., 2015). Zhang et al. (2007a), Zhang et al. (2007b) selected individual minerals from Zhijin and analyzed their REEs, giving ΣREE contents of small shell fossils and bioclasts of 60.6–156 ppm and 348–358 ppm, respectively, and those of dolomite matrix of 5.62–52.2 ppm. The ΣREE contents of the studied francolite grains range from 778 to 1451 ppm in our samples (Fig. 5D). As biological fossils or detritus are not major mineral phases, and the REE content in dolomite matrix is extremely low, it can be inferred that abundant REEs occur in francolite grains (Fig. 5D).

Element content maps can be used to examine the variation in element contents in minerals, thereby allowing insights into diagenesis (George et al., 2015). Our results show that the contents of REEs in francolite grains are much higher than those in dolomite matrix (Table 3). It should be noted that there is no obvious variation in REE content in francolite grains, with no pronounced content gradient between the core and the edge; rather, REEs are uniformly distributed in francolite grains, and there are no independent REE minerals, as

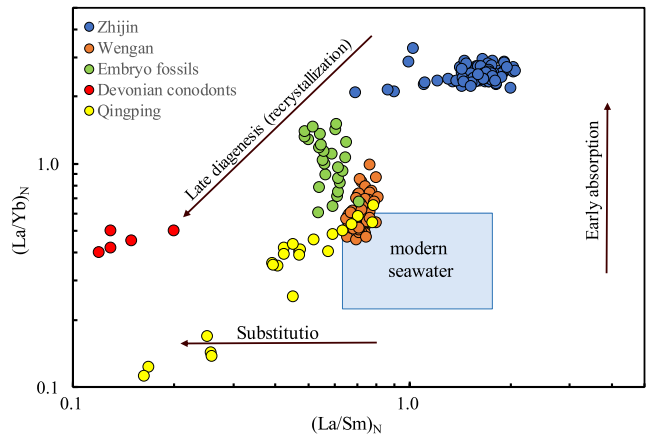

Fig. 9. Compilation of normalized $(La/Yb)_N$ ratios versus $(La/Sm)_N$ ratios of francolite grains from the Zhijin region plotted in the diagram proposed by Reynard et al. (1999). $(La/Sm)_N$ ratios are similar to those of modern seawater, whereas $(La/Yb)_N$ ratios are universally higher, as indicated by position with respect to the vertical arrow indicating adsorption.

established by analysis of our polished thin-sections using SEM (Fig. 3G–H). American Love Hollow phosphorite has the same characteristics (Emsbo et al., 2015). It is generally accepted that REEs occur in francolite in isomorphic form (Shi et al., 2004; Zhao et al., 2013; Chen et al., 2015; Liu et al., 2016; Guo et al., 2017; Lou and Gu, 2019). However, Liu et al. (2006) found an extremely rare fluorocerite, measuring only 2.6 μm in size, in Zhijin phosphorite. In addition, hydrothermally altered apatite may be accompanied by the formation of monazite or xenotime, which occur as inclusions in apatite (e.g., Harlov and FÖrster, 2003; Li and Zhou, 2015). However, the size of these inclusions may be less than one micrometer, which cannot be observed using traditional analytical methods.

5.3.2. Enrichment period of REEs

The topology of shale-normalized REE profiles in authigenic and biogenic phosphates is often used as an indicator of REE behavior in seawater (Garnit et al., 2012; Emsbo et al., 2015; Joosu et al., 2015; Gadd et al., 2016). For this to be effective, the timing of phosphorus formation must be synsedimentary (i.e., authigenic) rather than late diagenesis, as REE characteristics can be modified during the latter (Reynard et al., 1999; Lécuyer et al., 2004). Reynard et al. (1999) proposed that the REE profiles of francolite grains may reflect the quantitative absorption of REEs from the surrounding seawater or may reflect adsorption and substitution processes after deposition. A comparison of the partition coefficients of REEs in apatite and water for different mechanisms (absorption and substitution) suggests that the $(La/Sm)_N$ vs $(La/Yb)_N$ diagram proposed by Reynard et al. (1999) can be used to explain the different mechanisms of REE incorporation in apatite. The adsorption mechanism is determined by surface crystal chemistry, in which LREEs are preferentially adsorbed onto the surfaces of apatite crystals, and this process occurs mainly during early diagenesis (Reynard et al.,1999; Lécuyer et al., 2004; Gadd et al., 2016). The ratio of $(La/Yb)_N$ is not affected during the process of substitution, but the ratio of $(La/Yb)_N$ increases when the adsorption mechanism is dominant. In contrast, the ratio of $(La/Sm)_N$ usually remains unchanged during the absorption process but decreases during the process of substitution (Zhu and Jiang, 2017).

The relative contribution of adsorption or substitution mechanisms to REE contents in apatite can be quantitatively assessed by calculating the ratios of $(La/Yb)_N$ and $(La/Sm)_N$ (Renard et al., 1999; Garnit et al., 2012; Gadd et al., 2016). The mean $(La/Yb)_N$ ratio of francolite grains from Zhijin ranges from 2.08 to 3.27, and the mean $(La/Sm)_N$ ratio ranges from 0.69 to 2.07 (Table 4; Fig. 9). Reynard et al. (1999) and Gadd et al. (2016) proposed that a value of $(La/Yb)_N$ below 2.5 indicates

only slight adsorption during early diagenesis. Our data indicate that early diagenesis modified the distribution of LREEs with respect to HREEs. Similarly, the $(La/Sm)_N$ ratio can reveal the fractionation of LREEs with respect to MREEs; Lécuyer et al. (2004) suggested that ratios of > 0.3 are most likely initial REE values or only slightly changed, whereas ratios of < 0.3 indicate a marked addition of REEs (by substitution) into the crystal structure. For example, Devonian conodonts in phosphorite are inferred to have undergone a wide range of replacement mechanisms during late diagenesis (Fig. 9; Reynard et al., 1999). The mean $(La/Sm)_N$ ratio of francolite grains from Zhijin is >0.5, indicating that late substitution did not modify the pattern of primary LREEs/MREEs. These various lines of evidence together suggest that REE contents of the Zhijin phosphorite were influenced only by early diagenetic processes and not by late substitution.

5.3.3. Ultramicroscopic petrographic evidence for REE enrichment

BSE images revealed that the surfaces of francolite grains contain numerous small cracks and pores caused by long-term transportation and abrasion (Fig. 3G–H). However, the absence of reaction rims and hydrothermal erosion features suggests that the studied francolite grains did not undergo obvious hydrothermal transformation after diagenesis, supporting the results of geochemical analysis that REEs were enriched during early diagenesis. However, experimental studies and investigations into magmatic–hydrothermal REE deposits have demonstrated that tiny REE mineral inclusions can form through later fluid/hydrothermal alteration of apatite via coupled dissolution–reprecipitation (Harlov et al., 2002, 2005; Harlov and FÖrster, 2003; Li and Zhou, 2015). TEM is undoubtedly the best means to identify and characterize these tiny inclusions, as it can provide microstructural, crystallographic, and compositional information from micrometer- to sub-nanometer-sized regions of thin samples (Lee, 2010). Focused ion beam (FIB) instruments have been used extensively by geologists to prepare electron-transparent specimens (sections) of rock samples for imaging and chemical analysis at high spatial resolutions by TEM (e.g., Wirth 2004; Lee et al., 2007; Gerald et al., 2017). To determine whether the studied francolite contained these tiny inclusions, two FIB sections were prepared from representative francolite grains from Zhijin (Fig. 6a).

Apatite may recrystallize when eroded by hydrothermal fluids, and during the reaction of synthetic hydroxyapatite powder and natural fluorapatite with lead nitrate, needle-shaped epitaxially growing crystals may exchange cations at crystal interfaces (Kamiishi and Utsunomiya, 2013). Our FIB sections under TEM show that abundant nano-apatites with well-developed crystalline forms are adsorbed together and regular in shape, with a length of 50–200 nm; these apatites show denaturation by extrusion, but without connected crystals or recrystallization (Fig. 6b–e). These francolite nano-crystals lack obvious alteration interfaces or recrystallization with acicular structure. In the Yinachang Deposit, strong REE leaching occurred during alteration of REE-rich fluorapatite, and the REE minerals crystallized to form inclusions close to the location of leaching, with sharp compositional interfaces being formed between the altered and unaltered regions at a scale of micrometers (Li and Zhou, 2015). However, BSE imaging under a TEM excludes the existence of large particle inclusions in our samples, as revealed through electron pattern diffraction analysis of each region (Fig. 6f–g). In addition, no nano-inclusions were found, further ruling out the possibility that REEs were derived mainly from independent minerals or inclusions. Clearly, therefore, REEs substituted for Ca in the francolite lattice of the Zhijin deposit samples, similar to other phosphorites (Jarvis et al., 1994; Piper, 1999; Emsbo et al., 2015).

The geological processes that control REE contents in phosphate ores continue to be a topic of debate. The abundance of REEs and their content variation in francolite are thought to be related to sedimentary facies, grain size, burial time, and depth (Ilyin, 1998; Shield and Stille, 2001; Shields and Webb, 2004; Emsbo et al., 2015). However, recent studies have suggested that the enrichment of REEs in francolite crystal

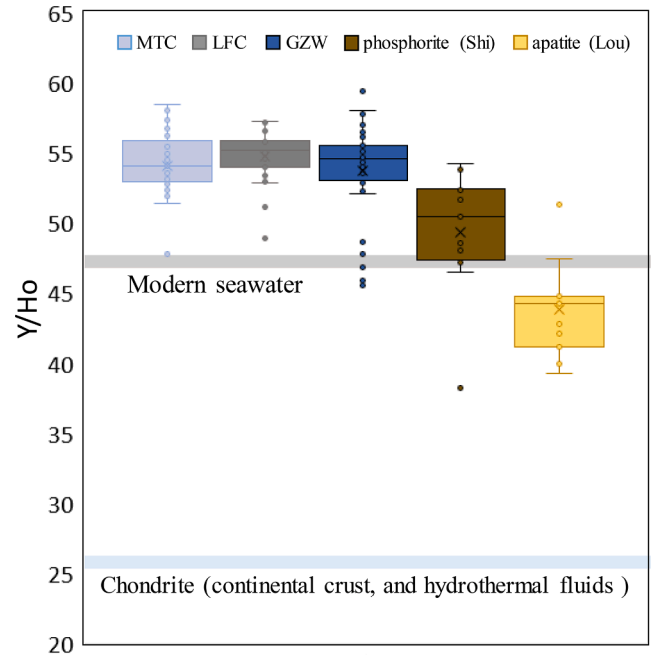

Fig. 10. Y/Ho data for francolite grains and fluids from different sources, after Gadd et al. (2016). Abbreviations: MS – modern seawater; CMH – continental crust, mantle, and high-temperature hydrothermal fluids.

lattice is controlled by the duration of exposure to seawater as well as mineral crystal porosity, meaning that francolite grains with large surface areas accumulate REEs more quickly and to a higher degree (Koeppenkastrop and De Carlo, 1992; Reynard et al., 1999; Auer et al., 2017). Laboratory studies have also suggested that REE scavenging takes place over a time frame of only several hours (Koeppenkastrop and De Carlo, 1992). The francolite grains from the Zhijin phosphorite underwent transport and abrasion before deposition, and the francolite might have been exposed to seawater for a prolong period during the crystallization and transport stages. TEM images reveal that francolite grains are aggregates of numerous nano-crystals, and this structure causes the specific surface area to be unusually large, which would favor REE enrichment. In addition, MREEs are preferentially incorporated into the crystal lattice during exposure to ocean water, resulting in a hat-shaped REE pattern (Koeppenkastrop and De Carlo, 1992; Sholkovitz et al., 1994), which is consistent with the REEs pattern of our samples (Fig. 5B, C).

5.4. REE sources of the Zhijin phosphorite

5.4.1. Geochemistry

A number of studies have shown that the content of Sr is an important indicator for evaluating the degree of diagenetic alteration, including the influence of atmospheric diagenesis and dolomitization (Kaufman and Knoll, 1995). Under the influence of meteoric fluids, Sr is expelled while Mn is incorporated by substituting for Ca^{2+} in the carbonate lattice until equilibrium is reached (Kaufman and Knoll, 1995; Hou et al., 2016). Derry et al. (1989) proposed that the minimum Sr content for Sr isotope stratigraphy is 200 ppm. Almost all of the measured Sr contents of the studied phosphorite samples from Zhijin are >200 ppm (mean of 561 ppm) (Fig. 11A). The MgO content of the sample showing a lower Sr content than this threshold was 17.65%, meaning that the main mineral of this sample is dolomite. Kaufman et al. (1992), Kaufman et al. (1993) and Derry et al. (1992) considered that a reliable Sr isotope value must satisfy the condition of Mn/Sr < 2–3, and samples with high Sr contents and low Mn/Sr ratios (<2–3) are generally considered better indicators of the diagenetic environment

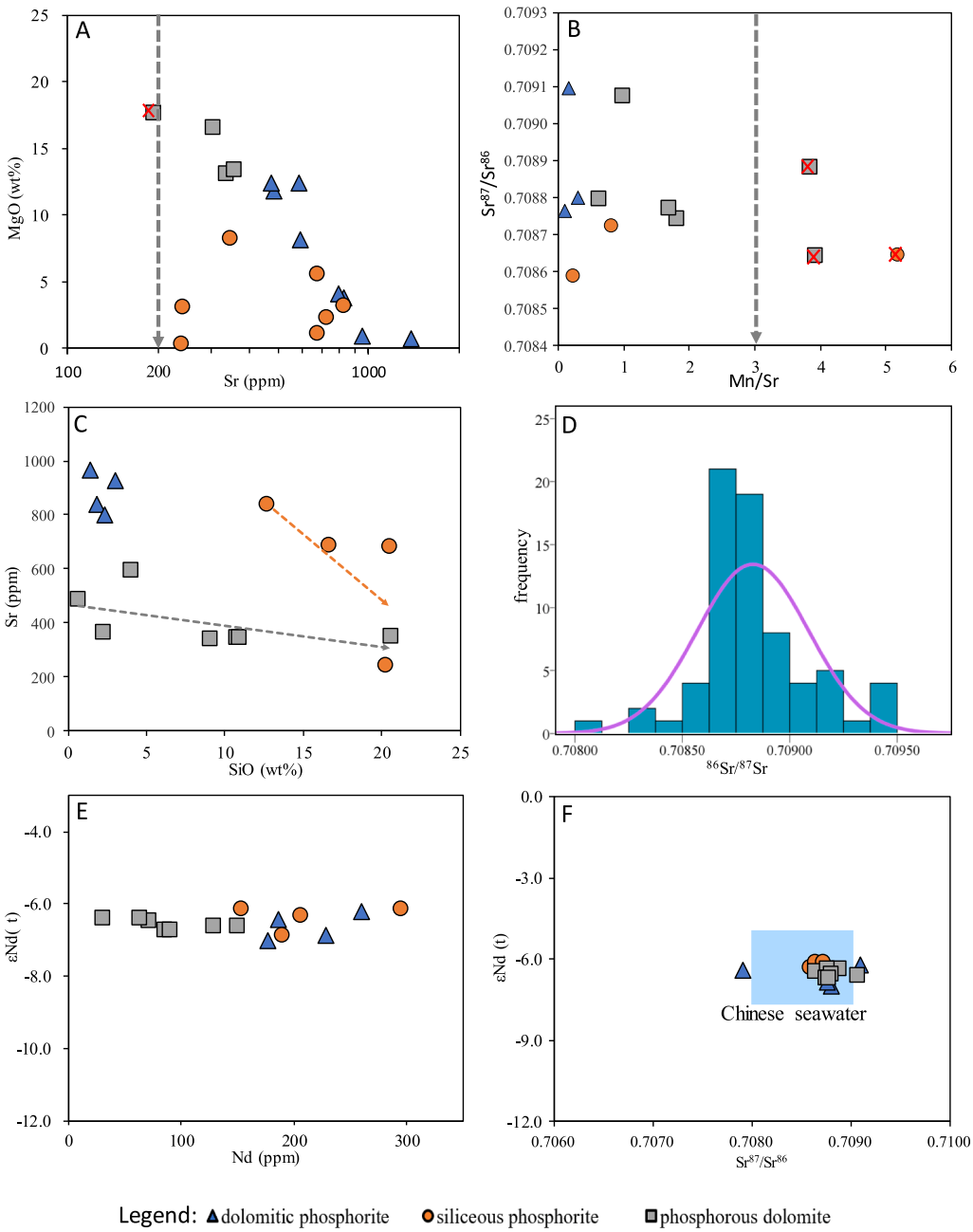

Fig. 11. Plots of the Sr–Nd isotopic composition of phosphorite samples from Zhijin. (A) Cross-plot of MgO vs. Sr for phosphorite samples from Zhijin; the red line represents an Sr concentration of 200 × 10^{-6}. (B) Cross-plot of $^{87}Sr/^{86}Sr$ vs. Mn/Sr, after Edwards et al. (2015); the red line represents an Mn/Sr value of 3. (C) Sr–SiO diagram for different phosphorites. (D) Normal distribution of $^{87}Sr/^{86}Sr$ ratio in francolite grains from Zhijin. (E–F) Cross-plots of εNd(t) vs. Nd and εNd(t) vs. $^{87}Sr/^{86}Sr$ ratio for phosphorite samples from Zhijin.

(Kaufman et al., 1993; Montañez et al., 1996). The Mn/Sr ratio for Zhijin phosphorite ranges from 0.09 to 5.16 (mean. 1.42), and there is no correlation between Mn and Sr. Consequently, the phosphorite from Zhijin should record the geochemical nature of the diagenetic environment.

The element Y is similar to REEs in terms of geochemical characteristics, and francolite grains from the Zhijin samples are also rich in Y: francolite from the GZW, LFC, and MTC shows Y contents of 364–521 ppm, 430–548 ppm, and 451–645 ppm, respectively (Table 3). In surface water, Y is depleted, but the concentration increases with increasing water depth in modern seawater, with Y/Ho values ranging from 47 to 77 (Bau, 1994; Gadd et al., 2016). The elements Ho and Y have the same or similar ionic radius and atomic valence, but in the marine environment, Ho is scavenged preferentially over Y by hydrogenous ferromanganese oxyhydroxide particles, resulting in a markedly higher Y/Ho value in the marine environment than in the continental crust, mantle, or high-temperature hydrothermal fluid (i.e., 26; Bau, 1994; Koschinsky et al., 1997; Gadd et al., 2016). The contents of Y in the GZW, LFC, and MTC are high and are characterized by positive anomalies. Values of the Y/Ho ratio are within the seawater range, at 45.6–59.4, 48.8–57.3, and 47.7–58.5 for the GZW, LFC, and MTC, respectively (Fig. 10). This suggests that the REEs in the studied francolite were sourced predominantly from ancient seawater. Furthermore, the hat-shaped distribution pattern of REEs observed for the Zhijin samples is interpreted to have been caused by the preferential uptake of MREEs into the crystal lattice during exposure to seawater (Koeppenkastrop and De Carlo, 1992; Sholkovitz et al., 1994), supporting the proposal that the source of REEs was early Cambrian seawater.

5.4.2. Sr isotopes

The residence time of Sr in the ocean ranges from 2.5 to 4 Myr at present (Palmer and Edmond, 1989; Hodell et al., 1990; Melezhik et al., 2001), which is much longer than that of surface and thermohaline ocean circulation (~10^3 years) (Brooker, 1982). Therefore, if a well-

preserved marine authigenic composition can be determined and appropriate dissolution methods are used, the Sr isotope composition in the whole ocean can be considered relatively uniform (Melezhik et al., 2001; Li et al., 2011). Marine carbonate and phosphate deposits studied using this method can inherit the $^{87}Sr/^{86}Sr$ ratio of the sedimentary environment without secondary (diagenetic and epigenetic) alteration and retain the original Sr isotopic characteristics (Kuznetsov et al., 2018). The $^{87}Sr/^{86}Sr$ compositions of phosphorite in the Zhijin region should reflect the global change in $^{87}Sr/^{86}Sr$ because the Yangtze platform was connected to an open ocean during the early Cambrian (Fan et al., 2016). The Sr contents of different types of Zhijin phosphorite samples also show negative correlations with the contents of SiO_2 (Fig. 11C) and MgO, suggesting that Sr in the sample was mainly from francolite, followed by dolomite matrix and silica.

The Sr isotopic compositions of dolomite and phosphorite can be used to reconstruct the $^{87}Sr/^{86}Sr$ value in the Precambrian ocean (Kuznetsov et al., 2018). The $^{87}Sr/^{86}Sr$ values of the studied dolomitic phosphorite, siliceous phosphorite, and phosphorous dolomite range from 0.7079 to 0.7091, 0.7085 to 0.7109, and 0.7086 to 0.7091, respectively. Also, the in situ $^{87}Sr/^{86}Sr$ values of the francolite range from 0.7081 to 0.7095 (mean of 0.7088; Fig. 11D). The $^{87}Sr/^{86}Sr$ ratios of Uchur–Maya and the region of Siberia (540–553 Ma) are 0.70812–0.70823 and 0.70829–0.70844, respectively (Derry et al., 1994; Semikhatov et al., 2003); those for Namibia (549–543 Ma) measured by Kaufman et al. (1993) are 0.70840–0.70858; and those for phosphorite in southern China are 0.70837–0.70852 (Sawaki et al., 2010). Values of $^{87}Sr/^{86}Sr$ in Chinese seawater were between 0.7080 and 0.7090 during the Cambrian (Derry et al., 1994;). The $^{87}Sr/^{86}Sr$ values of the studied Zhijin phosphorite samples are the same as the global seawater value at that time, implying that the metallogenic material of the francolite was likely derived from the paleo-ocean.

This higher $^{87}Sr/^{86}Sr$ value during the Cambrian (compared with other geological periods) can be observed in other continents of the world and is considered a global rather than a regional or local marine phenomenon (Sawaki et al., 2008, 2014; Halverson et al., 2010). During the Neoproterozoic, especially the early Cambrian, accompanied by the breakup of the Rodinia supercontinent and global glaciation, an increase in the intensity of weathering resulted in an increase in the $^{87}Sr/^{86}Sr$ value of seawater (Powell et al., 1993; Shields, 2007; Halverson et al., 2010). Considering the relationship between $^{87}Sr/^{86}Sr$ value and weathering intensity in seawater, the abrupt increase in continental weathering conditions during the early Cambrian may explain the extreme positive $^{87}Sr/^{86}Sr$ excursion then, which might have made a substantial contribution to the radiogenic $^{87}Sr/^{86}Sr$ composition of marginal shallow basins (Richter et al., 1992; Kasemann et al., 2014).

The disintegration of the Super-continent Rodinia was considered to have some relationships with the continuous increase of $^{87}Sr/^{86}Sr$ in the paleo-seawater (Shields, 2007). Due to the increase of physical weathering rate caused by tectonic uplift, the overall chemical weathering rate during super-continent rupture and micro-continent collision became higher (Gaillard et al., 1999; Jacobsen and Kaufman, 1999; Squire et al., 2006). The Cambrian period stands out as a prominent period when the increase of chemical weathering rate and continental weathering pushed the earth system to a new state (Squire et al., 2006; Shields, 2007). It has been preliminarily confirmed that the super-continent breakup affected the circulation of CO_2 in the atmosphere and hydrosphere, changed the global climate in the late Precambrian, and further intensified the deposition of carbonate, iron, manganese and phosphorus in the lithosphere surface (Powell et al., 1993; Bloch et al., 2006; Shields, 2007; Halverson et al., 2010). During the period of 800–543 Ma, over 100 phosphorite deposits were developed on the earth (Holland, 2005). Therefore, the clastic materials produced by continental weathering might have provided abundant primary metallogenic materials for the Zhijin deposit.

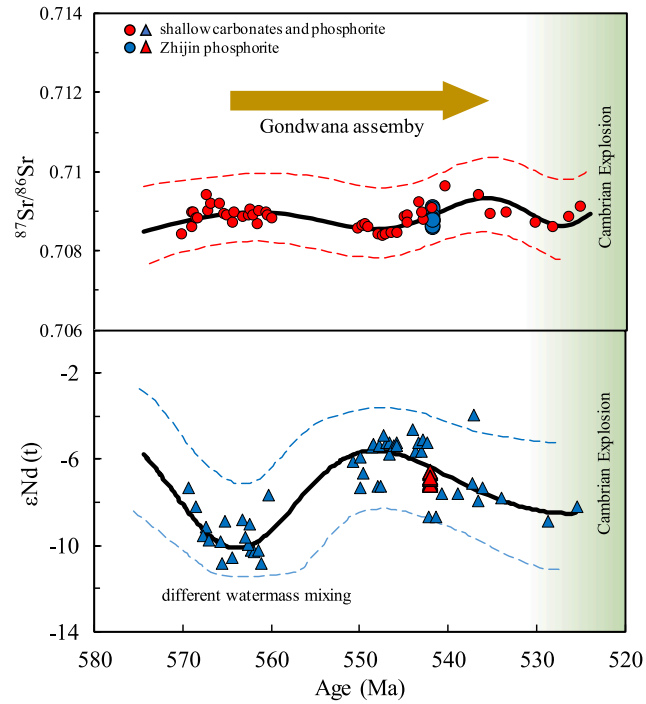

Fig. 12. Covariation in εNd(t) and $^{87}Sr/^{86}Sr$ of shallow carbonates and phosphorites during the early Cambrian (modified after Wei et al., 2019). Blue circles and red triangles represent data for Zhijin phosphorites.

5.4.3. Nd isotopes

Values of εNd(t) for the dolomitic phosphorite samples vary from − 6.99 to − 6.21, with the siliceous phosphorite samples and the phosphorous dolomite samples showing distinct ranges of − 6.33 to − 6.14 and − 6.73 to − 6.37, respectively. The value of εNd(t) of seawater in China decreased from − 4.5 during the early Sinian to − 8.0 during the early Cambrian. The negative εNd(t) values indicate that a continental crust source was the main source of REEs in seawater. Owing to continental weathering, terrigenous detrital sediment may be transported to the ocean through rivers. Geochemically, Nd is highly particle reactive, and its incorporation into mineral is essentially completed during early diagenesis. The εNd(t) value is the most important indicator of the surrounding water of francolite, as it tracks the change in Nd isotopic composition of pore water during the formation of phosphorites (Michard et al., 1985; Martin and Scher, 2004; Xin et al., 2015). Secular variation in shallow seawater εNd(t) values is a direct result of changes in weathered materials exported to the continental shelf area, driven by long-term tectonic activity (Wei et al., 2019). The variation in $^{87}Sr/^{86}Sr$ and εNd(t) of the early Cambrian (Fig. 12) might have been related to the breakup of Rodinia and the subsequent assembly of Gondwana, which intensified the influx of terrigenous clastic materials into the shallow sea. Isotopic evidence reveals that the metallogenic material was derived from paleo-seawater (Fig. 11F), meaning that shallow seawater with abundant terrigenous detritus in Zhijin was an ideal environment for the formation of phosphate deposits.

5.5. Enrichment mechanism of REEs

On the basis of the results presented above, we divided the enrichment of REEs in Zhijin francolite grains into three stages: the crystallization, transportation, and sedimentation stages (Fig. 13). During the early Cambrian, accompanied by the breakup of the Rodinia supercontinent and global glaciation, an increase in the intensity of weathering resulted in an increase in the amount of metallogenic material contained in seawater (Shields, 2007; Halverson et al., 2010). In the crystallization stage, during crystal growth, francolite obtained the initial REEs from

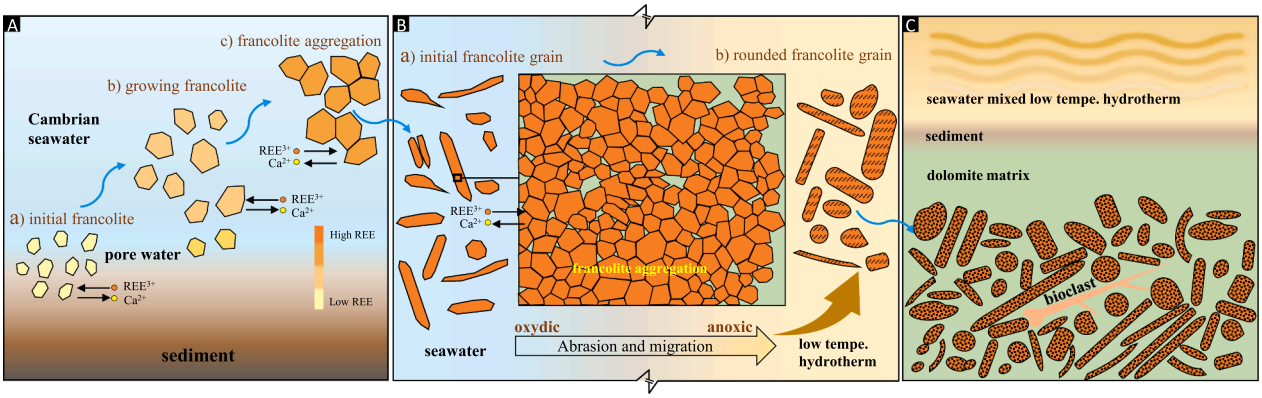

Fig. 13. Schematic diagrams illustrating the REE mineralization and sedimentation of francolite grains in the Zhijin deposit. (A) Crystallization stage of francolite, characterized by growth and aggregation of nano-crystals, and substitution of Ca^{2+} by REE^{3+} in seawater in the francolite lattice. (B) Transport and abrasion stage of francolite, characterized by aggregation of nano-crystals of francolite to form francolite grains, following which the grains were abraded by hydrodynamic force and transported to the shallow sea at Zhijin, where they were mixed with low-temperature hydrothermal fluids. (C) Hydrothermal–sedimentary stage of phosphorite, with some bioclasts being buried in the phosphorite.

the surrounding oxidic seawater in the form of lattice substitution (Fig. 13a). Strong hydrodynamic action forced francolite crystals to migrate and be aggregated into primary francolite grains (Yang and He, 2013; Liu et al., 2016). In the transportation stage, under the influence of intensifying ocean currents and sea waves, these francolite grains were abraded and transported to the coastal area, where the enrichment of REEs was completed (Fig. 13b). During this process, the long-term exposure to seawater and the high specific surface area of apatite particles contributed to their obtention of abundant REEs in paleo-seawater (Koeppenkastrop and De Carlo, 1992; Reynard et al., 1999; Auer et al., 2017). In the sedimentary stage, the low-temperature hydrothermal solution mixed with seawater to form an anoxic environment (Quan et al., 2007; Liu et al., 2019; Zhang et al., 2019), and francolite grains and some bioclastics were buried and deposited in the Zhijin region (Fig. 13c).

6. Conclusion

The Zhijin REE-associated phosphorus deposit is a hydrothermal–sedimentary deposit in which the enrichment of REEs occurred before sedimentation. The REEs in Zhijin phosphorite occur mainly in francolite grains, which are aggregates of numerous nanoscale francolite crystals. The francolite grains were enriched with REEs during the early diagenetic stage and were abraded and transported in seawater before sedimentation.

Our study focused on establishing the occurrence, enrichment mechanism, and source of REEs in francolite grains. REEs occur in francolite crystals in isomorphic form, as mineral inclusions and independent REE minerals are not found in these grains. Francolite grains were enriched in REEs from seawater during the diagenetic stage before sedimentation. The prolonged exposure time in seawater of francolite grains and their high specific Sawaki et al. (2008), Sawaki et al. (2014) surface area favored REE enrichment of the Zhijin phosphorite. Hydrothermal–sedimentary mineralization made no distinct contribution to REE enrichment. The direct source of REEs in francolite grains was paleo-seawater rather than hydrothermal fluids, and the REEs in seawater were sourced ultimately from terrigenous detrital material.

Uncited references

.

Declaration of Competing Interest

The authors declare that they have no known competing financial interests or personal relationships that could have appeared to influence the work reported in this paper.

Acknowledgments

This research was supported by the National Key R&D Program of China (Grant 2017YFC0602301), the National Key R&D Program of China (Grant 2017YFC0602300) and the National Science Foundation for Young Scientists of China (Grant 41702085). We sincerely thank the experimenters and engineers Changming Xing, Dan Wu in the Key Laboratory of Mineralogy and Metallogeny, Chinese Academy of Sciences for help with the requisite experiments. This is contribution No.IS-3051 from GIGCAS

References

Adams, J.A.S., Weaver, C.E., 1958. Thorium-to-uranium ratios as indicators of sedimentary processes: Example of concept of geochemical facies. AAPG Bull. 42 (2), 387–430.
Anderson, R.F., Fleisher, M.Q., LeHuray, A.P., 1989. Concentration, oxidation state, and particulate flux of uranium in the Black Sea. Geochim. Cosmochim. Acta 53 (9), 2215–2224.
Auer, G., Reuter, M., Hauzenberger, C.A., Piller, W.E., 2017. The impact of transport processes on rare earth element patterns in marine authigenic and biogenic phosphates. Geochim. Cosmochim. Acta 203, 140–156.
Bajwah, Z., Seccombe, P., Offler, R., 1987. Trace element distribution Co: Ni ratios and genesis of the Big Cadia iron-copper deposit, New South Wales, Australia. Miner. Deposita 22, 292–300.
Bau, M., Dulski, P., 1996. Distribution of yttrium and rare-earth elements in the Penge and Kuruman iron-formations, Transvaal Supergroup, South Africa. Precambr. Res. 79 (1-2), 37–55.
Bau, M., 1994. Evolution of the yttrium-holmium systematics of seawater through time. Mineral. Mag. 58A (1), 61–62.
Berner, R.A., Beerling, D.J., Dudley, R., Robinson, J.M., Wildman, J., Richard, A., 2003. Phanerozoic atmospheric oxygen. Annu. Rev. Earth Planet. Sci. 31, 105–134.
Bertram, C.J., Elderfield, H., Aldridge, R.J., Conway Morris, S., 1992. 87Sr/86Sr, 143Nd/144 Nd and REEs in Silurian phosphatic fossils. Earth Planet. Sci. Lett. 113 (1-2), 239–249.
Bloch, J.D., Timmons, J.M., Crossey, L.J., Gehrels, G.E., Karlstrom, K.E., 2006. Mudstone petrology of the mesoproterozoic unkar group, grand canyon, U.S.A.: Provenance, weathering, and sediment transport on intracratonic rodinia. J. Sediment. Res. 76 (9), 1106–1119.
Boström, K., 1983. Genesis of ferromanganese deposit diagnostic criteria for recent and old deposits. Springer, Boston.
Breit, G.N., Vanty, R.B., 1991. Vanadium accumulation in carbonaceous rocks: A review of geochemical controls during and deposition and diagenesis. Chem. Geol. 91, 83–97.
Broecker, W.S., 1982. Ocean chemistry during glacial time. Geochim. Cosmochim. Acta 46 (10), 1689–1705.
Bright, C.A., Cruse, A.M., Lyons, T.W., MacLeod, K.G., Glascock, M.D., Ethington, R.L., 2009. Seawater rare-earth element patterns preserved in apatite of Pennsylvanian conodonts. Geochim. Cosmochim. Acta 73 (6), 1609–1624.
Chen, J., Algeo, T.J., Zhao, L., Chen, Z.-Q., Cao, L., Zhang, L., Li, Y., 2015. Diagenetic uptake of rare earth elements by bioapatite, with an example from Lower Triassic conodonts of South China. Earth-Sci. Rev. 149, 181–202.
Chen, J.Y., Yang, R.D., Zhang, J., 2010. Mode of occurrence of rare earth elements in posphorite in Zhijin County, Guizhou Province. China. Acta mineralogica sinca. 30 (01), 123–129.

Chen, L., Zhong, H., Hu, R.Z., Xiao, J.F., Zou, Y.R., 2006. Early Cambrian oceanic anoxic event in northern Guizhou biomarkers and organic carbon isotope. Acta Petrologica Sinica. 22(9), 2413-2423.
Chen, X.P., Gao, J.Y., Chen, D.F., Dong, W.Q., 1992. The concept of hydrothermal sedimentation and its petrologieal Criteria. Acta sedimentologica since. 03, 124–132.
De Baar, H.J.W., Bacon, M.P., Brewer, P.G., 1985. Rare earth elements in Pacific and Atlantic Oceans. Geochim. Cosmochim. Acta. 49, 1943–1959.
Derry, L.A., Brasier, M.D., Corfield, R.M., Rozanov, A.Y., Zhuravlev, A.Y., 1994. Sr and C isotopes in Lower Cambrian carbonates from the Siberian craton: A paleoenvironmental record during the 'Cambrian explosion'. Earth Planet. Sci. Lett. 128 (3-4), 671–681.
Derry, L.A., Kaufman, A.J., Jacobsen, S.B., 1992. Sedimentary cycling and environmental change in the Late Proterozoic: evidence from stable and radiogenic isotopes. Geochim. Cosmochim. Acta 56 (3), 1317–1329.
Derry, L.A., Keto, L.S., Jacobsen, S.B., Knoll, A.H., Swett, K., 1989. Sr isotopic variations in upper Proterozoic carbonates from Svalbard and east Greenland. Geochim. Cosmochim. Acta 53 (9), 2331–2339.
Dill, H., 1986. Metallogenesis of early Paleozoic graptolite shales from the Graefenthal Horst (Northern Bavaria—Federal Republic of Germany). Economic Geology. 81, 889-903.
Dill, H., Kemper, E., 1990. Crystallographic and chemical variations during pyritization in the upper Barremian and lower Aptian dark claystones from the Lower Saxonian Basin (NW Germany). Sedimentology 37 (3), 427–443.
Dulski, P., 1994. Interferences of oxide, hydroxide and chloride analyte species in the determination of rare earth-elements in geological samples by inductively-coupled plasma-mass spectrometry. Fresenius J. Anal. Chem. 350 (4-5), 194–203.
Edwards, C.T., Saltzman, M.R., Leslie, S.A., Bergström, S.M., Sedlacek, A.R.C., Howard, A., Bauer, J.A., Sweet, W.C., Young, S.A., 2015. Strontium isotope (87Sr/86Sr) stratigraphy of Ordovician bulk carbonate: Implications for preservation of primary seawater values. Geol. Soc. Am. Bull. 127 (9-10), 1275–1289.
Elderfield, H., Greaves, M.J., 1982. The rare earth elements in seawater. Nature 296 (5854), 214–219.
Elderfield, H., Pagett, R., 1986. Rare earth elements in ichthyoliths: Variations with redox conditions and depositional environment. Sci. Total Environ. 49, 175–197.
Emsbo, P., McLaughlin, P.I., Breit, G.N., du Bray, E.A., Koenig, A.E., 2015. Rare earth elements in sedimentary phosphate deposits: Solution to the global REE crisis? Gondwana Res. 27 (2), 776–785.
Fan, H., Wen, H., Zhu, X., 2016. Marine redox conditions in the early cambrian Ocean: Insights from the Lower Cambrian Phosphorite Deposits, South China. J. Earth Sci. 27 (2), 282–296.
Francois, R., 1988. A study on the regulation of the concentrations of some trace metals (Rb, Sr, Zn, Pb, Cu, V, Cr, Ni, Mn and Mo) in Saanich Inlet Sediments, British Columbia, Canada. Marine Geology. 1988, 83(1-4), 285-308.
Follmi, K., 1996. The phosphorus cycle, phosphogenesis and marine phosphaterich deposits. Earth-Sci. Rev. 40 (1-2), 55–124.
Gadd, M.G., Layton-Matthews, D., Peter, J.M., 2016. Non-hydrothermal origin of apatite in SEDEX mineralization and host rocks of the Howard's Pass district, Yukon, Canada. Am. Mineral. 101 (5), 1061–1071.
Garnit, H., Bouhlel, S., Barca, D., Chtara, C., 2012. Application of LA-ICP-MS to sedimentary phosphatic particles from Tunisian phosphorite deposits: insights from trace elements and REE into paleo-depositional environments Chemie der Erde - Geochemistry - Interdisciplinary. J. Chem. Prob. Geosci. Geoecol. 72 (2), 127–139.
George, L., Cook, N.J., Ciobanu, C.L., Wade, B.P., 2015. Trace and minor elements in galena: A reconnaissance LA-ICP-MS study. Am. Mineral. 100 (2-3), 548–569.
German, C.R., Elderfield, H., 1990. Application of the Ce anomaly as a paleoredox indicator: The ground rules. Paleoceanography 5 (5), 823–833.
Grandjean, P., Cappetta, H., Michard, A., Albarede, F., 1988. The asssment of REEs patterns and 143 Nd/144 Nd ratio in fish remains. Earth Planet. Sci. Lett. 84, 181–196.
Gregory, D.D., Large, R.R., Halpin, J.A., Baturina, E.L., Lyons, T.W., Wu, S., Danyushevsky, L., Sack, P.J., Chappaz, A., Maslennikov, V.V., Bull, S.W., 2015. Trace element content of sedimentary pyrite in black shales. Econ. Geol. 110 (6), 1389–1410.
Gui, K., Zhen, Y.Y., 1987. Study on the sedimentary environments of the Sinian and Camberian phosphorite in South China. Acta Sedimentologica Sinca. 1, 1–9.
Guo, H.Y., Xia, Y., He, S., Xie, Z.J., Wei, D.T., Lei, B., 2017. Geochemical characteristics of Zhijin phosphorite type rare-earth deposit, Guizhou Province, China. Acta mineralogic Sinca. 6 (37), 81–89.
Guy, B.M., Beukes, N.J., Gutzmer, J., 2010. Paleoenvironmental controls on the texture and chemical composition of pyrite from nonconglomeratic sedimentary rocks of the Mesoarchean Witwatersrand Supergroup, South Africa. S. Afr. J. Geol. 113 (2), 195–228.
Halverson, G.P., Wade, B.P., Hurtgen, M.T., Barovich, K.M., 2010. Neoproterozoic chemostratigraphy. Precambr. Res. 182 (4), 337–350.
Hannigan, R.E., Sholkovitz, E.R., 2001. The development of middle rare earth element enrichments in freshwaters: weathering of phosphatic minerals. Chem. Geol. 175, 495–508.
Harlov, D.E., Förster, H.J., Nijland, T.G., 2002. Fluidinduced nucleation of REE-phosphate minerals in apatite: Nature and experiment Part I. Chlorapatite. Am. Mineral. 87, 245–261.
Harlov, D.E., FÖrster, H.J., 2003. Fluid-induced nucleation of REE phosphate minerals in apatite: nature and experiment. Part II. Fluorapatite. American Mineralogist. 88, 1209-1229.
Hatch, J.R., Leventhal, J.S., 1992. Relationship between inferred redox potential of the depositional environment and geochemistry of the Upper Pennsylvanian (Missourian) Stark Shale Member of the Dennis Limestone, Wabaunsee County, Kansas, U.S.A. Chemical Geology. 99(1–3), 65-82.
Hodell, D.A., Mead, G.A., Mueller, P.A., 1990. Variation in the strontium isotopic composition of seawater (8 Ma to present): implications for chemical weathering rates and dissolved fluxes to the oceans. Chem. Geol. 80 (4), 291–307.
Holland, H.D., 2005. 100th anniversary special paper: Sedimentary mineral deposits and the evolution of Earth's Near-Surface Environments. Econ. Geol. 100 (8), 1489–1509.
Hou, M.C., Jiang, W.J., Xing, F.C., Xu, S.L., Liu, X.C., Xiao, C., 2016. Origin of dolomites in the Cambrian (Upper 3rd-Furongian) formation. South-Eastern Sichuan Basin, China, Geofluids. 16 (5), 856–876.
Huston, D.L., Sie, S.H., Suter, G.F., Cooke, D.R., Both, R.A., 1995. Trace elements in sulfide minerals from eastern Australian volcanic-hosted massive sulfide deposits, Part II. Selenium levels in pyrite: Comparison with 34S values and implications for the source of sulfur in volcanogenic hydrothermal systems. Econ. Geol. 90 (5), 1167–1196.
Ilyin, A.V., 1998. Rare-earth geochemistry of 'old' phosphorites and probability of syngenetic precipitation and accumulation of phosphate. Chem. Geol. 144, 243–256.
Jacobsen, S.B., Kaufman, A.J., 1999. The Sr, C and O isotopic evolution of Neoproterozoic seawater. Chem. Geol. 161 (1-3), 37–57.
Jarvis, I., Burnett, W.C., Nathan, Y., Almbaydin, F.S.M., Attia, A.K.M., Castro, L.N., Flicoteaux, R., Hilmy, M.E., Husain, V., Qutawnah, A.A., Serjani, A., Zanin, Y.N., 1994. Phosphorite geochemistry—state-of-the-art and environmental concerns. Eclogae Geologicae Helvetiae (Journal of the Swiss Geological Society). 87, 643–700.
Jia, Z.B., Hou, D.J., Sun, D.Q., Jiang, Y.H., Zhao, Z., Zhang, Z.M., Hong, M., Chang, Z., Dong, L.C., 2018. Characteristics and geological implications of rare earth elements in black shale in hydrothermal sedimentation areas: A case study from the Lower Cambrian Niutitang Fm shale in central and eastern Guizhou. Nat. Gas. Ind. 38 (5), 44–51.
Jiang, S.-Y., Zhao, H.-X., Chen, Y.-Q., Yang, T., Yang, J.-H., Ling, H.-F., 2007. Trace and rare earth element geochemistry of phosphate nodules from the lower Cambrian black shale sequence in the Mufu Mountain of Nanjing, Jiangsu Province, China. Chem. Geol. 244 (3-4), 584–604.
Jones, B., Manning, D.A.C., 1994. Comparison of geochemical indices used for the interpretation of depositional environments in ancient mudstones. Chem. Geol. 111, 112–129.
Joosu, L., Lepland, A., Kirsimäe, K., Romashkin, A.E., Roberts, N.M.W., Martin, A.P., Črne, A.E., 2015. The REE-composition and petrography of apatite in 2 Ga Zaonega Formation, Russia: The environmental setting for phosphogenesis. Chem. Geol. 395, 88–107.
Kamiishi, E., Utsunomiya, S., 2013. Nano-scale reaction processes at the interface between apatite and aqueous lead. Chem. Geol. 340, 121–130.
Kasemann, S.A., Pogge von Strandmann, P.A.E., Prave, A.R., Fallick, A.E., Elliott, T., Hoffmann, K.-H., 2014. Continental weathering following a Cryogenian glaciation: Evidence from calcium and magnesium isotopes. Earth Planet. Sci. Lett. 396, 66–77.
Kaufman, A.J., Knoll, A.H., Awramik, S.M., 1992. Biostratigraphic and chemostratigraphic correlation of Neoproterozoic sedimentary successionns: Upper Tindir Group, northwestern Canada, as a test case. Geology 20, 181–185.
Kaufman, A., Knoll, A., 1995. Neoproterozoic variations in the C-isotopic composition of seawater: stratigraphic and biogeochemical implications. Precambr. Res. 73 (1-4), 27–49.
Kaufman, A.J., Jacobsen, S.B., Knoll, A.H., 1993. The Vendian record of Sr- and C-isotopic variations in seawater: implications for tectonics and paleoclimate. Earth Planet. Sci. Lett. 120 (3-4), 409–430.
Kidder, D., Krishnaswamy, R., Mapes, R.H., 2003. Elemental mobility in phosphatic shales during concretion growth and implication for provenance analysis. Chem. Geol. 198, 335–353.
Kimura, H., Watanabe, Y., 2001. Oceanic anoxia at the Precambrian-Cambrian boundary. Geology 29 (11), 995.
Koeppenkastrop, D., De Carlo, E.H., 1992. Sorption of rare-earth elements from seawater onto synthetic mineral particles: an experimental approach. Chem. Geol. 95 (3-4), 251–263.
Koschinsky, A., Stascheit, A., Bau, M., Halbach, P., 1997. Effects of phos¬phatization on the geochemical and mineralogical composition of marine fer¬romanganese crusts. Geochim. Cosmochim. Acta 61 (19), 4079–4094.
Kuznetsov, A.B., Semikhatov, M.A., Gorokhov, I.M., 2018. Strontium Isotope Stratigraphy: Principles and State of the Art. Stratigr. Geol. Correl. 26 (4), 367–386.
Large, R.R., Maslennikov, V.V., Robert, F., Danyushevsky, L.V., Chang, Z., 2007. Multistage Sedimentary and Metamorphic Origin of Pyrite and Gold in the Giant Sukhoi Log Deposit, Lena Gold Province, Russia. Econ. Geol. 102 (7), 1233–1267.
Lee, M.R., 2010. Transmission electron microscopy (TEM) of Earth and planetary materials: A review. Mineral. Mag. 74 (1), 1–27.
Lee, M.R., Brown, D.J., Smith, C.L., Hodson, M.E., MacKenzie, M., Hellmann, R., 2007. Characterization of mineral surfaces using FIB and TEM: A case study of naturally weathered alkali feldspars. Am. Mineral. 92 (8-9), 1383–1394.
Lécuyer, C., Reynard, B., Grandjean, P., 2004. Rare earth element evolution of Phanerozoic seawater recorded in biogenic apatites. Chem. Geol. 204 (1-2), 63–102.
Lewan, M.D, 1984. Factors controlling the proportionality of vanadium to nickel in crude oils. Geochim. Cosmochim. Acta 48 (11), 2231–2238.
Lewan, M.D., Maynard, J.B., 1982. Factors controlling enrichment of vanadium and nickel in the bitumen of organic sedimentary rocks. Geochim. Cosmochim. Acta 46 (12), 2547–2560.
Li, D., Zhou, S., G., Ling, H.F., Thirlwall, M., 2011. Dissolution methods for strontium isotope stratigraphy: Guidelines for the use of bulk marine carbonate and phosphorite rocks. Chemical Geology. 290(3-4), 133-144.

Li, X., Zhou, M.-F., 2015. Multiple stages of hydrothermal REE remobilization recorded in fluorapatite in the Paleoproterozoic Yinachang Fe–Cu–(REE) deposit, Southwest China. Geochimica Et Cosmochimica Acta. 166, 53–73.
Ling, H.-F., Chen, X., Li, D., Wang, D., Shields-Zhou, G.A., Zhu, M., 2013. Cerium anomaly variations in Ediacaran–earliest Cambrian carbonates from the Yangtze Gorges area, South China: implications for oxygenation of coeval shallow seawater. Precambr. Res. 225, 110–127.
Liu, J., Wen, H.J., Liu, H.R., Fan, H.F., Zhang, Y.X., 2016. Structures and Sedimentary Environment of Phosphorite in Zhijin County, Guizhou Province, China. Acta mineralogic Sinca. 036 (002), 253–259.
Liu, S.R., Hu, R.Z., Yao, L.B., Zhou, G.F., 2006. Independent rare earth minerals were found for the first time in Xinhua phosphate deposit, Zhijin, Guizhou. Acta mineralogica since. 26 (1), 118.
Liu, S.R., 2008. Study of the Mineralization Process of Zhijin Xinhua Phosphate Deposit Using Microbeam Analyses. Institute of Geochemistry, Chinese Academy of Sciences.
Liu, X.Q., Zhang, H., Tang, Y., Liu, Y.L., 2019. Effect of hydrothermal process on the Zhijin phosphorite-type REE deposit in Guizhou Province: evidence from fluid inclusions. Acta Mineralogica Sinica. 39 (04), 403–411.
Lou, F.J., Gu, S.Y., 2019. LA-ICP-MS REE analyses for phosphates and dolomites in Cambrian phosphorite in Zhijin, Guizhou Province: implication for depositional conditions and diagenetic processes. J. Chin. Rare Earth Soc. 38 (2), 225–323.
Marchig, V., 1982. Some geochemistry indicators for discrimination between diagenetic and hydrotgermal metalliferous sediments. Mar. Geol. 58 (3), 241–256.
Martin, E.E., Scher, H.D., 2004. Preservation of seawater Sr and Nd isotopes in fossil fish teeth: Bad news and good news. Earth Planet. Sci. Lett. 220 (1-2), 25–39.
Michard, A, Gurriet, P, Soudant, M, Albarede, F, 1985. Nd isotopes in French Phanerozoic shales: external vs. internal aspects of crustal evolution. Geochim. Cosmochim. Acta 49 (2), 601–610.
McArthur, J.M., Walsh, J.N., 1984. Rare-earth geochemistry of phosphorites. Chem. Geol. 47 (3-4), 191–220.
Montañez, I.P., Banner, J.L., Osleger, D.A., Borg, L.E., Bosserman, P.J., 1996. Integrated Sr isotope variations and sea level history of middle to upper Cambrian platform carbonates: implications for the evolution of Cambrian seawater 87Sr/86Sr. Geology 24 (10), 917. https://doi.org/10.1130/0091-7613(1996)024<0917:ISIVAS>2.3.CO;210.1130/9654.
Melezhik, V.A., Gorokhov, I.M., Fallick, A.E., Gjelle, S., 2001. Strontium and carbon isotope geochemistry applied to dating of carbonate sedimentation: an example from high-grade rocks of the norwegian caledonides. Precambr. Res. 108 (3), 267–292.
Moysiuk, J., Smith, M.R., Caron, J.B., 1989. Hyoliths are Palaeozoic lophophorates. Nature 541 (7637), 394–398.
Palmer, M.R., Edmond, J.M., 1989. The strontium isotope budget of the modern ocean. Earth Planet. Sci. Lett. 92 (1), 11–26.
Picard, S., Lécuyer, C., Barrat, J.-A., Garcia, J.-P., Dromart, G., Sheppard, S.M.F., 2002. Rare earth element contents of Jurassic fish and reptile teeth and their potential relation to seawater composition (Anglo-Paris Basin, France and England). Chem. Geol. 186 (1-2), 1–16.
Pi, D.H., Liu, C.Q., Zhou, S., Graham, A., Jiang, S.Y., 2013. Trace and rare earth element geochemistry of black shale and kerogen in the early Cambrian Niutitang Formation in Guizhou province, South China: Constraints for redox environments and origin of metal enrichments. Precambr. Res. 225, 218–229.
Piper, D.Z., Baedecker, P.A., Crock, J.G., Burnett, W.C., Loebner, B.J., 1988. Rare earth elements in the phosphatic-enriched sediment of the Peru shelf. Mar. Geol. 80 (3-4), 269–285.
Piper, D.Z., 1999. Trace elements and major element oxides in the Phosphoria Formation at Enoch Valley, Idaho-Permian sources and current reactivities. U.S. Geological Survey Open-File. Report. 99–163.
Powell, C. McA., Li, Z.X., McElhinny, M.W., Meert, J.G., Park, J.K., 1993. Paleomagnetic constraints on timing of the Neoproterozoic breakup of Rodinia and the Cambrian formation of Gondwana. Geology 21 (10), 889. https://doi.org/10.1130/0091-7613(1993)021<0889:PCOTOT>2.3.CO;210.1130/9335.
Qiu, K.F., Yu, H.C., Wu, M.Q., Geng, J.Z., Ge, X.K., Gou, Z.Y., Taylor, R.D., 2019. Discrete Zr and REE mineralization of the Baerzhe rare-metal deposit, China. Am. Mineral. 104 (10), 1487–1502.
Qiu, K.F., Yu, H.C., Hetherington, C., Huang, Y.Q., Yang, T., Deng, J., 2020. Tourmaline composition and boron isotope signature as a tracer of magmatic-hydrothermal processes. American Mineralogist.
Quan, G.L., Ma, Y.Q., Li, X.K., Gao, K.M., Xie, J.T., 2007. Overview on the geochemical characteristic of Sinian-Cambrian Phosphorite in Guizhou. 2007, 264–269.
Radhika, S., Nagaphani Kumar, B., Lakshmi Kantam, M., Ramachandra Reddy, B., 2011. Solvent extraction and separation of rare-earths from phosphoric acid solutions with TOPS 99. Hydrometallurgy 110 (1-4), 50–55.
Reynard, B., Lécuyer, C., Grandjean, P., 1999. Crystal-chemical controls on rare-earth element concentrations in fossil biogenic apatites and implications for paleoenvironmental reconstructions. Chem. Geol. 155 (3-4), 233–241.
Richter, F.M., Rowley, D.B., DePaolo, D.J., 1992. Sr isotope evolution of seawater: the role of tectonics. Earth Planet. Sci. Lett. 109 (1-2), 11–23.
Rimmer, S.M., 2004. Geochemical paleoredox indicators in Devonian-Mississippian black shales, Central Appalachian Basin (USA). Chem. Geol. 206 (3-4), 373–391.
Ross, D. J.K., Bustin, R.M., 2006. Sediment geochemistry of the Lower Jurassic Gordondale Member, northeastern British Columbia. Bull. Can. Pet. Geol. 54 (4), 337–365.
Runnegar, B., 2000. Loophole for snowball Earth. Nature 405 (6785), 403–404.
Sawaki, Y., Ohno, T., Fukushi, Y., Komiya, T., Ishikawa, T., Hirata, T., Maruyama, S., 2008. Sr isotope excursion across the Precambrian-Cambrian boundary in the Three Gorges area, South China. Gondwana Res. 14 (1-2), 134–147.
Sawaki, Y., Ohno, T., Tahata, M., Komiya, T., Hirata, T., Maruyama, S., Windley, B.F., Han, J., Shu, D., Li, Y., 2010. The Ediacaran radiogenic Sr isotope excursion in the Doushantuo Formation in the Three Gorges area, South China. Precambri. Res. 176 (1-4), 46–64.
Sawaki, Y., Tahata, M., Ohno, T., Komiya, T., Hirata, T., Maruyama, S., Han, J., Shu, D., 2014. The anomalous Ca cycle in the Ediacaran ocean: Evidence from Ca isotopes preserved in carbonates in the Three Gorges area, South China. Gondwana Res. 25 (3), 1070–1089.
Semikhatov, M.A., Ovchinnikova, G.V., Gorokhov, I.M., Kuznetsov, A.B., Petrov, P.Y., 2003. Pb-Pb isochron age and Sr-isotopic signature of the Upper Yudoma carbonate sediments (Vendian of the Yudoma–Maya trough, Eastern Siberia). Doklady Earth Sci. 393 (8), 1093–1097.
Shi, C.H., 2005. Formation of phosphorite deposits, breakup of Rodinia supercontinent and biology explosion: a case study of Weng'an. Kaiyang and Zhijin phosphprite deposits of Guizhou Province, Graduate School of Chinese Academy of Sciences (Institute of Geochemistry).
Shields, G., Stille, P., 2001. Diagenetic constraints on the use of cerium anomalies as palaeoseawater redox proxies: An isotopic and REE study of Cambrian phosphorites. Chem. Geol. 175 (1-2), 29–48.
Shields, G.A., 2007. A normalised seawater strontium isotope curve: possible implications for Neoproterozoic-Cambrian weathering rates and the further oxygenation of the Earth. Earth 2 (2), 35–42.
Shields, G.A., Webb, G.E., 2004. Has the REE composition of seawater changed over geological time. Chem. Geol. 204 (1-2), 103–107.
Sholkovitz, E.R., Landing, W.M., Lewis, B.L., 1994. Ocean particle chemistry: The fractionation of rare earth elements between suspended particles and seawater. Geochim. Cosmochim. Acta 58 (6), 1567–1579.
Squire, R., Campbell, I., Allen, C., Wilson, C., 2006. Did the Transgondwanan Supermountain trigger the explosive radiation of animals on Earth? Earth Planet. Sci. Lett. 250 (1-2), 116–133.
Stalder, M., Rozendaal, A., 2004. Apatite nodules as an indicator of depositional environment and ore genesis for the Mesoproterozoic Broken Hill-type Gamsberg Zn–Pb deposit, Namaqua Province, South Africa. Mineral Deposita. 39 (2), 189–203.
Sverjensky, D.A., 1984. Europium redox equilibria in aqueous-solution. Earth Planet. Sci. Lett. 67 (1), 70–78.
Taylor, S.R., McLennan, S.M., 1985. The Continental Crust: Its Composition and Evolution. Blackwell Scientific Publications, Oxford.
Thomas, H.V., Large, R.R., Bull, S.W., Maslennikov, V., Berry, R.F., Fraser, R., Froud, S., Moye, R., 2011. Pyrite and pyrrhotite textures and composition in sediments, laminated quartz veins, and reefs at bendigo gold mine, australia: insights for ore genesis. Econ. Geol. 106 (1), 1–31.
Webb, G.E., Kamber, B.S., 2000. Rare earth elements in Holocene reefal microbialites: A new shallow seawater proxy. Geochim. Cosmochim. Acta 64 (9), 1557–1565.
Wei, H.Y., 2012. Sedimentary geology and Tethyan geology. Sedimentary Geol. Tethyan Geol. 32 (02), 76–88.
Wei, G.-Y., Ling, H.-F., Shields, G.A., Chen, T., Lechte, M., Chen, X., Qiu, C., Lei, H., Zhu, M., 2019. Long-term evolution of terrestrial inputs from the ediacaran to early Cambrian: clues from Nd isotopes in shallow-marine carbonates, South China. Palaeogeogr. Palaeoclimatol. Palaeoecol. 535, 109367. https://doi.org/10.1016/j.palaeo.2019.109367.
Wen, H.J., Jean, C., Zhang, Y.X., Fan, H.F., Christophe, C., Liu, S.R., 2011. Molybdenum isotopic records across the Precambrian-Cambrian boundary. Geology. 39(8), 775-778.
Wignall, P.B., Twitchett, R.J., 1996. Oceanic anoxia and the end permian mass extinction. Science 272 (5265), 1155–1158.
Wright, J., Schrader, H., Holser, W.T., 1987. Paleoredox variations in ancient oceans recorded by rare earth elements in fossil apatite. Geochim. Cosmochim. Acta 51 (3), 631–644.
Wirth, R., 2004. Focused Ion Beam (FIB): A novel technology for advanced application of micro- and nanoanalysis in geosciences and applied mineralogy. Eur. J. Mineral. 16 (6), 863–876.
Wu, M.Q., Samson, I.M., Qiu, K.F., Zhang, D.H., 2021. Concentration mechanisms of REE-Nb-Zr-Be mineralization in the Baerzhe deposit, NE China: Insights from textural and chemical features of amphibole and rare-metal minerals. Econ. Geol. 116 (03), 651–679.
Xu, J.B., Xiao, J.F., Yang, H.Y., Xia, Y., 2019. The REE enrichment characteristics and constraints of the phophorite in Zhijin, Guizhou: A case study of No. 2204 drilling cores in the Motianchong ore block. Acta Mineralogica Sinca. 39 (04), 29–37.
Yang, J., He, T.Y., 2013. Zhijin county Guizhou Province Xinhua containing rare earth phosphate rock deposit geological characteristics and reasons discussed. Geol. Chem. Min. 35 (1), 27–33.
Zhang, J., Sun, C.M., Gong, M.L., Zhang, Q., Chen, D.L., Cheng, J.Y., 2007a. Geochemical Characteristics and Occurrence States of the REE Elements of the Phosphorite in Xinhua, Zhijin, Guizhou. Chinese Rare Earths. 01, 75–79.
Zhang, J., Zhang, T., Chen, D.L., 2003. REE Geochemmistry of the Ore-Bearing REE in Xinhua Phosphorite, Zhijin, Guizhou. J. Mineral. Petrol. 03, 35–38.
Zhang, Y.B., Gong, M.L., Li, H., 2007b. Occurrence of REE in Rare Earth Phosphorite in Zhijin Area, Guizhou. J. Earth Sci. Environ. 04, 362–368.
Zhang, Y.S., Zhang, J., Mao, R.Y., 2019. REE composition and tracing characteristics of lower cambrian black shale in Guizhou. Chinese Rare Earths. 40 (03), 7–19.
Zhao, L., Chen, Z.-Q., Algeo, T.J., Chen, J., Chen, Y., Tong, J., Gao, S., Zhou, L., Hu, Z., Liu, Y., 2013. Rare-earth element patterns in conodont albid crowns: Evidence for massive inputs of volcanic ash during the latest Permian biocrisis? Global Planet. Change 105, 135–151.
Zhao, Z.H., 2016. Principle of trace element geochemistry. Science Press, Beijing.

Zhu, B., Jiang, S.Y., Yang, J.H., Pi, D.H., Ling, H.F., Chen, Y.Q., 2014. Rare earth element and Sr–Nd isotope geochemistry of phosphate nodules from the lower Cambrian Niutitang Formation, NW Hunan Province, South China. Palaeogeography Palaeoclimatol. Palaeoecol. 398 (3), 132–143.

Zhu, B., Jiang, S.Y.A., 2017. LA-ICP-MS analysis of rare earth elements on phosphatic grains of the Ediacaran Doushantuo phosphorite at Weng'an, South China: implication for depositional conditions and diagenetic processes. Geol. Mag. 1–17.

Zhou, K.L., Fu, Y., Ye, Y.M., Long, K.S., Zhou, W.X., 2019. Characteristics of the REE enrichment of the Early Cambrian phosphorus-rich rocks in Guizhou Province, China. Acta Mineralogica Sinica. 4, 420–430.